The nature of faint radio galaxies at high redshifts

A. Saxena[1]⋆, H. J. A. Röttgering[1], K. J. Duncan[1], P. N. Best[2], G. J. Hill[3],
B. L. Indahl[3], M. Marinello[4], R. A. Overzier[4,5], L. Pentericci[6], I. Prandoni[7],
H. Dannerbauer[8,9] and R. T. Genova Santos[8]

[1] *Leiden Observatory, Leiden University, P.O. Box 9513, 2300 RA Leiden, The Netherlands*
[2] *Institute for Astronomy, University of Edinburgh, Royal Observatory, Blackford Hill, Edinburgh EH9 3HJ, UK*
[3] *McDonald Observatory & Department of Astronomy, University of Texas at Austin, 1 University Station, Austin, TX 78712, USA*
[4] *Observatoório Nacional, Rua General José Cristino, 77, São Cristóvão, Rio de Janeiro, RJ, CEP 20921-400, Brazil*
[5] *Institute of Astronomy, Geophysics and Atmospheric Sciences, Department of Astronomy, University of São Paulo,*
São Paulo, SP 05508-090, Brazil
[6] *INAF-Osservatorio Astronomico di Roma, Via Frascati 33, I-00040 Monteporzio (RM), Italy*
[7] *INAF-Instituto di Radioastronomia, Via P. Gobetti 101, I-40129 Bologna, Italy*
[8] *Instituto de Astrofísica de Canarias (IAC), E-38205 La Laguna, Tenerife, Spain*
[9] *Universidad de La Laguna, Dpto. Astrofísica, E-38206 La Laguna, Tenerife, Spain*

ABSTRACT

We present spectra and near-infrared images of a sample of faint radio sources initially selected as promising high-redshift radio galaxy (HzRG) candidates. We have determined redshifts for a total of 13 radio galaxies with redshifts ranging from $0.52 \leq z \leq 5.72$. Our sample probes radio luminosities that are almost an order of magnitude fainter than previous large samples at the highest redshifts. We use near-infrared photometry for a subsample of these galaxies to calculate stellar masses using simple stellar population models, and find stellar masses to be in the range $10^{10.8} - 10^{11.7} M_\odot$. We then compare our faint radio galaxies with brighter radio galaxies at $z \geq 2$ from the literature. We find that fainter radio galaxies have lower Lyα luminosities and narrower full width at half maxima compared to the bright ones, implying photoionisation by weaker AGN. We also rule out the presence of strong shocks in faint HzRGs. The stellar masses determined for faint HzRGs are lower than what has been observed for brighter ones. We find that faint HzRG population in the redshift range $2 - 4$ forms a bridge between star-forming and narrow-line AGN, whereas the ones at $z > 4$ are dominated by star-formation, and may be building up their stellar mass through cold accretion of gas. Finally, we show that the overall redshift evolution of radio sizes at $z > 2$ is fully compatible with increased inverse Compton scattering losses at high redshifts.

Key words: galaxies: high-redshift – galaxies: active

1 INTRODUCTION

High-redshift radio galaxies (HzRGs) have been found to be hosted by some of the most massive galaxies in the universe and are thought to be progenitors of the massive ellipticals we observe today. HzRGs contain large amounts of dust and gas (Best et al. 1998b; Archibald et al. 2001; Carilli et al. 2002; Reuland et al. 2004; De Breuck et al. 2010), are dominated by an old stellar population (Best et al. 1998a; Rocca-Volmerange et al. 2004; Seymour et al. 2007) and seen to

have high star formation rates (Willott et al. 2003; McLure et al. 2004; Miley et al. 2006; Villar-Martín et al. 2007a; Seymour et al. 2008). Owing to the large stellar masses of their host galaxies, radio-loud AGN across all redshifts are often found to be located in the centre of clusters and proto-clusters (Pentericci et al. 2000; Venemans et al. 2002; Röttgering et al. 2003; Miley et al. 2004; Hatch et al. 2011; Wylezalek et al. 2013; Orsi et al. 2016). Miley & De Breuck (2008) summarise the properties of radio galaxies and their environments in their review.

HzRGs are seen to be some of the most massive galaxies across all redshifts (see Rocca-Volmerange et al. 2004,

⋆ E-mail: saxena@strw.leidenuniv.nl

for example). As a result, near-infrared magnitudes of radio galaxies have been observed to follow a correlation with redshift, which is known as the $K - z$ relation (Jarvis et al. 2001b; Willott et al. 2003; Rocca-Volmerange et al. 2004). This is mainly because of the consistently high stellar masses observed and because HzRGs are thought to be dominated by an old stellar population, and the K band traces the part of SED that contains light emitted from these old stars. At higher redshifts ($z > 4$), the scatter in the $K - z$ relation is seen to increase as bluer parts of the rest-frame SED containing light from younger stars (which is more sensitive to the star-formation history) are observed in the K band.

Selecting HzRGs based on their radio emission alone has the advantage that no prior colour selection (one that probes the Lyman break, for example) is applied (De Breuck et al. 2000a). In principle, promising high-redshift candidates selected from a radio survey with follow-up optical/IR spectroscopy could discover massive galaxies all the way into the epoch of reionisation through observations of their redshifted synchrotron spectrum. Since radio observations are not affected by dust, radio selected galaxies can also provide an unbiased sample to study the dust properties of galaxies at high redshifts.

A successful method of identification of HzRGs from all-sky radio surveys is to first create samples of radio sources that display an ultra-steep spectral index (α, where $S \propto \nu^\alpha$) and then follow these up at optical and infrared wavelengths (Tielens et al. 1979; Röttgering et al. 1994; Chambers et al. 1996; Blundell et al. 1999; De Breuck et al. 2000a; Ishwara-Chandra et al. 2010; Afonso et al. 2011; Singh et al. 2014). This method is effective owing to the apparent correlation that exists between the redshift of a radio source and the steepness of its low-frequency radio spectrum (see Ker et al. 2012, for example). The physical explanation for this correlation is still under debate, but it is commonly accepted that curvature of the radio SED combined with a K-correction is responsible for the apparent correlation. For a more thorough discussion on the redshift-spectral index correlation, we point the readers to Miley & De Breuck (2008) where some other possible explanations are also discussed. From an observational point of view, however, radio sources with an ultra-steep spectrum (USS) generally make promising HzRG candidates. Most of the currently known radio galaxies at the highest redshifts have been selected from relatively shallow all-sky surveys. Therefore, the well-studied HzRG samples (van Breugel et al. 1999; Willott et al. 1999; De Breuck et al. 2000a; Rawlings et al. 2001; Jarvis et al. 2001a; Willott et al. 2003; Vardoulaki et al. 2010; Rigby et al. 2011) mostly consist of luminous radio sources, and very little is currently known about the fainter and presumably more abundant radio galaxies at high redshifts. With the advent of the latest generation of radio telescopes such as the upgraded Giant Metrewave Radio Telescope (*GMRT*; Swarup et al. 1991), the Low Frequency Array (*LOFAR*; van Haarlem et al. 2013), the Murchinson Widefield Array (*MWA*; Tingay et al. 2013) and the Square Kilometer Array (*SKA*; Dewdney et al. 2009) in the future, it is now possible to survey large areas of the sky to unprecedented depths at low radio frequencies and push the discovery of radio galaxies to lower luminosities and/or to higher redshifts, well into the epoch of reionisation (EoR; $z > 6$).

The spectra of radio galaxies across all redshifts are rich with emission lines and there have been many studies exploring the primary source of photoionisation in radio galaxies and AGN using UV and optical emission lines and their ratios. Robinson et al. (1987) and Baum et al. (1992) found that photoionisation by the central AGN alone was found to sufficiently explain the UV and optical line ratios observed in low redshift radio galaxies ($z < 0.2$). However, for radio galaxies at higher redshifts, photoionisation by AGN was not enough to explain the observed blue colours and bright Lyα emission observed in these objects (Villar-Martin et al. 1997). Further, there is evidence of strong interaction between the radio jet and the interstellar medium (ISM) of the host galaxy, that leads to the generation of powerful shocks that disturb the morphology, kinematics and physical conditions of the line-emitting gas (van Ojik et al. 1996; McCarthy et al. 1996; Villar-Martin et al. 1997). This interaction is also supported by observations that show close alignment between the radio jet and the extended emission line regions of HzRGs (Miley et al. 1992; Jannuzi et al. 1995). More recently, observations of the alignment of molecular gas with the radio jet in distant radio galaxies has lent further support to the jet-gas interaction scenario in radio galaxies (see Emonts et al. 2014, for example).

In this paper, we first present results from a campaign to spectroscopically follow-up the faint HzRG candidates identified by Saxena et al. (2018a) and observe a subset of these at near-infrared wavelengths. The layout of this paper is as follows. In Section 2 we present our new sample of spectroscopically confirmed radio galaxies. We first briefly describe the sample selection, observations and data reduction methods. We then present the spectroscopic and galaxy properties derived for the new radio galaxy sample, which probes fainter flux densities than previous all-sky radio surveys across all redshifts. In Section 3 we compile a list of known radio galaxies at $z > 2$ from the literature, and use this literature sample to compare the properties of the faint high-redshift radio galaxies presented in this paper. We explore various correlations between radio properties such as luminosity, size and spectral index with emission line properties such as line luminosity and widths in both the faint and literature HzRG samples. In Section 4 we present a discussion about the possible nature of faint HzRGs and offer an explanation for the overall trends observed in the radio galaxy samples. Finally, in Section 5 we summarise the key findings of this study.

Throughout this paper we assume a flat ΛCDM cosmology with $H_0 = 70$ km s^{-1} Mpc^{-1} and $\Omega_m = 0.3$.

2 THE FAINT HZRG SAMPLE

2.1 Sample selection

The HzRG candidates targeted for spectroscopy are mainly selected on the basis of (i) steepness of their spectral index ($\alpha_{1400}^{150} < -1.3$) calculated by cross-matching with the VLA FIRST survey at 1.4 GHz (Becker et al. 1995) and (ii) compact morphologies (largest angular size < 10 arcsec), which are expected from radio galaxies at the highest redshifts (Saxena et al. 2017). Lower flux density limits were applied both at 150 MHz and 1.4 GHz to ensure a high enough signal to noise ratios and upper flux density limits were applied
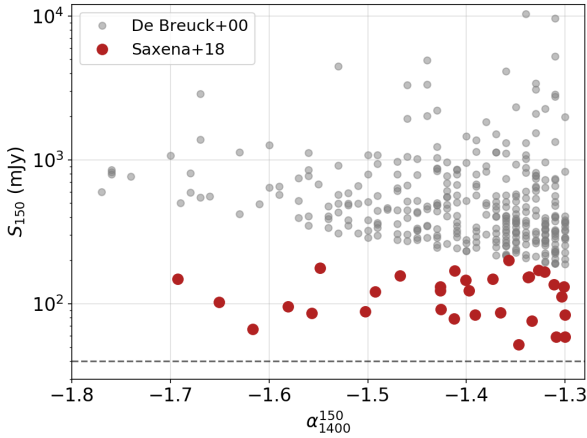
strategy was not practical and spectra had to be obtained over a long period of time, through multiple observing runs on numerous facilities around the world.

We used the long-slit setup with Gemini and WHT, and the integral field unit (IFU) setup with the HET. The typical observing times were one hour on source per object. The radio morphologies for most of the targets were unresolved (at a beam size of ~ 1.3 arcseconds and for these targets we aligned the slit at a parallactic angle of 0 degrees. For resolved radio objects, the slit was aligned along the extended radio morphology, as radio galaxy hosts are typically extended over a few arcseconds and often oriented along the radio axis (Röttgering et al. 1997). IFU observations were simply centred on the expected location of the radio host galaxy. Below we describe the observations taken using each telescope in detail. An overview of the setups used in various observing runs is given in Table 1.

2.2.1   4.2m William Herschel Telescope

The observations at the WHT were carried out using the Intermediate dispersion Spectrograph and Imaging System (ISIS[1]) instrument with a 3 arcminute slit length and a slit width of 1.5 arcseconds (Program IDs: W17AN014 and W19AN015, PI: Saxena). We used the R300B grating in the Blue arm and the R158R grating in the Red arm of the spectrograph, providing a spectral resolution of R ~ 975 and R ~ 910, respectively and a total spectral range of ~ 3200 to ~ 9200 over both arms. The first set of observations were carried out from 24 to 27 July 2017. The first two nights of the observing run were strongly affected by Saharan dust covering the island, leading to extinction of up to 2 mags in worst conditions. The conditions improved significantly for the final two nights. The average seeing over all four nights was around 0.6″. The second set of observations were carried out from from 3 to 5 March 2019. The average seeing for the first two nights was ~ 1.0″, and the third night was lost due to bad weather. During both runs, the same strategy for calibration was adopted, as described below.

Standard afternoon calibrations were performed and both dome and sky flats were taken before and after each observing night. A flux standard was observed at the beginning and the end of each night. Each target was observed for a total of 3600 (1800×2) seconds in each arm simultaneously, except when a bright line or continuum was spotted after the first 1800 seconds. In such cases the second exposure was terminated earlier. We used CuAr + CuNe lamps for wavelength calibration, which were observed at the position of each target before the sky exposure. Since the optical magnitudes of the targets are very faint ($R > 23.5$ AB), we first acquired a bright star close to the target and then added offsets to arrive at the target coordinates. This ensures accurate positioning of the slit for very faint targets. Standard data reduction procedures that include bias subtraction, flat fielding, sky subtraction, wavelength calibration and flux calibration were performed using PYTHON

Figure 1. The unique parameter space in flux density and spectral index probed by the Saxena et al. (2018a) sample of ultra-steep spectrum radio sources selected from TGSS ADR1. Shown for comparison are the radio sources from De Breuck et al. (2000a). Going to fainter flux densities should open up the potential for discovering radio galaxies at higher redshifts than seen before, and lead to the discovery of fainter radio galaxies at all redshifts, providing a more complete picture of the radio galaxy population.

at 150 MHz to ensure that none of the sources in our final sample would have been detected in previous searches for ultra-steep spectrum radio sources (for example De Breuck et al. 2000a). Further, only those sources with no clear optical or infrared counterparts in the available all-sky surveys such as SDSS (Alam et al. 2015), PanSTARRS1 (Chambers et al. 2016), ALLWISE (Wright et al. 2010), UKIDSS LAS (Lawrence et al. 2007) were retained in the final sample, increasing the likelihood of a high redshift nature of the radio host. The distribution of the selected sources in the radio flux density – spectral index parameter space (taken from Saxena et al. 2018a) is shown in Figure 1.

The final sample consisted of 32 radio sources that were followed up with the Karl G. Jansky Very Large Array (VLA) in configuration A in bands L and P (Project code: 16B-309, PI: Röttgering), with an average beam size of 1.3 arcseconds at 1.4 GHz (L-band). These results are presented in Saxena et al. (2018a). The high-resolution VLA images enabled sub-arcsecond isolation of the expected optical counterpart of the radio source. Blind spectroscopy at the position of the expected host of a radio source has been found to be successful at detecting emission lines and obtaining redshifts (Röttgering et al. 1994; De Breuck et al. 2001).

2.2   Observations and data reduction

Spectra presented in this paper were obtained over a period of December 2016 – March 2019 using three different telescopes, namely the 10m Hobby-Eberly Telescope (HET) at McDonald Observatory, Texas, the 8.2m Gemini North at Hawaii and the 4.2m William Herschel Telescope (WHT) at La Palma, Canary Islands. Due to the large distribution in right ascension of the sample, a homogeneous follow-up

---

[1] http://www.ing.iac.es/astronomy/instruments/isis/index.html

Table 1. Observational set-ups for spectroscopy used in this study.

Telescope	Instr.	Grism/Grating	λ coverage ()	Date	Exp. time (sec)	Limiting flux (1σ) (erg s^{-1} cm^{-2} Å^{-1})
WHT	ISIS	R300B/R158R	$3200 - 9200$	24 – 27 Jul. 2017	$1800 - 3600$	1.1×10^{-18}
				3 – 5 Mar. 2019	$3600 - 7200$	2.7×10^{-18}
Gemini North	GMOS	R400_G5305	$5600 - 9400$	7 Apr. – 24 Jun. 2017	2400	1.0×10^{-18}
HET	LRS2 IFU	LRS2-B/R	$3700 - 10500$	Dec. 2016 – Mar. 2018	3600	$2.0 - 7.0 \times 10^{-18}$

scripts written by our team. These scripts were based on the WHT data reduction package written by Steve Crawford[2].

2.2.2   8.2m Gemini North

The observations at Gemini North were carried out using the Gemini Multi-Object Spectrograph (GMOS; Hook et al. 2004) in long-slit mode with a slit width of 1.5″ and a slit length of 5 arcminutes (Program ID: GN-2017A-Q-8, PI: Overzier) . A total observing time of 7 hours was used to observe six targets. The observations were carried out over a period of two months, from 7 April 2017 to 24 June 2017. We used the R400_G5305 grating with a central wavelength of 700 nm, giving a resolution of $R \sim 1500$, providing coverage over the wavelength range 3600 – 9400 Å. We took three exposures of 800s each, giving 2400s of exposure time per object.

We used the Gemini IRAF package[3] for reducing the data, which performed all the basic reductions including bias subtraction, dark subtraction, flat-fielding and cosmic-ray removal. Wavelength and flux calibration was then performed on the spectra using the pipeline tools.

2.2.3   10m Hobby-Eberly Telescope (HET)

The observations at the HET were carried out using the Low Resolution Spectrograph 2 (LRS2; Lee et al. 2010), which is a 7×12 sq. arcsec fiber integral-field unit (IFU), covering a wavelength range of $3500 - 11000$ with a resolving power of $R \sim 1800$. The wavelength range on the LRS2 is split into two spectrographs, the LRS2-B ($3500 - 6300$) and LRS2-R ($6300 - 11000$). The observations were taken in spectroscopic sky conditions over four trimesters, beginning in December 2016 and ending in March 2018 (PI: Hill).

We used the LRS2 data reduction package[4] written in PYTHON to perform the basic reduction of the IFU data. The reduction steps include bad pixel masking, bias subtraction, flat fielding, cosmic ray removal and wavelength calibration using arc lamps (taken with either Cd, Hg, FeAr, or Kr) for individual frames from both blue and red arms. The reduced data products include both 2D row-stacked spectra (RSS) and 3D data cubes. The individual RSS and cubes were then median combined to form the final science data products.

Table 2. Number of objects observed and number of detections during spectroscopy runs on different telescopes. There are a few objects that have duplicate observations on multiple telescopes. We also count continuum detections in these numbers, but their spectra have not been presented in this study.

Telescope (code)	Observed	Detected	Percentage detected
WHT (W)	20	8	40%
Gemini North (G)	6	5	83%
HET (H)	15	8	54%

The presence of line emission in the data was first identified by visually examining the 2D spectra. Where signs of an emission line were spotted, we looked at the spatial distribution of the line emission in the 3D data cube. When the full spatial extent of the emission line was determined by eye, we used a circular aperture that fully encompassed the emitting region with a signal-to-noise of 3 or above, to extract the pixels with line emission. The 1D spectra from all pixels within the aperture were then median stacked to create a 1D spectrum of the source. The LRS2-B and -R response functions were then used to calibrate the flux of the extracted 1D spectrum and emission lines were then identified using methods that are described in the following section.

We observed different targets in each of our spectroscopy runs on the three different telescopes listed above but there were a few targets that were observed using two or more telescopes owing to scheduling restrictions. We list the number of targets observed and the number of detections, either emission lines or continuum, recorded during all our runs in Table 2. In the next section we summarise the flux limits achieved and detection rates from each of our observing runs.

2.2.4   Near-infrared imaging

Additional near-infrared (NIR) imaging in the *J* and *K* bands was obtained using LUCI (formerly known as LUCIFER; Seifert et al. 2003) on the Large Binocular Telescope for 9 HzRG candidates in our sample. Of these, 7 had spectroscopically confirmed redshifts. Below we highlight the observations and data reduction strategy.

The observations were carried out in two separate runs, with the first on 1 February 2018 and the second on 11 May 2018 (Program ID 2017 2018 43; PI: Prandoni). The average seeing throughout the observations was $0.6 - 1.0$ arcseconds. The average on-source exposure times were 720 (12×60s) seconds in *J* (central wavelength of 1.247 microns) and 1200 (20×60s) in *K* (central wavelength of 2.194 microns). We used a standard jitter pattern with a maximum jitter dis-

tance of 15 arcseconds to enable effective sky subtraction in both bands.

The LUCI data reduction pipeline developed at INAF-OAR was used to perform the reductions and calibrations of raw images. These tasks include dark subtraction, bad pixel masking, cosmic ray removal, flat-fielding, and sky subtraction. Astrometric corrections for individual frames were calculated and applied and the corrected frames were then resampled and combined using a weighted co-addition method to obtain a deep image. The photometry of the co-added image was then calibrated using 2MASS and where available, UKIDSS Large Area Survey to an accuracy of within 0.1 mag. The median and standard deviation of the background in all co-added images were then calculated by placing random apertures with a diameter of 1.5 arcseconds.

One source was observed using EMIR, a near-infrared imager/spectrograph (Garzon et al. 2004) on the Gran Telescopio Canarias (GTC) in queue mode (Proposal ID: 124-GTC85/17B, PI: Santos). The observation was taken in J and K bands, with 220 and 760 seconds of on-source exposure time, respectively. The average seeing for this observation was $1.0''$. Standard procedures for data reduction and calibrations of the raw images were performed, as mentioned previously.

2.3 Results

2.3.1 Flux limits and detection rates

The median 1σ flux limit achieved in the first observing run on WHT was 1.1×10^{-18} erg s^{-1} cm^{-2} Å^{-1}. We targeted 12 sources in total and were able to detect 7 (either emission lines or continuum). During the second observing run on the WHT, the conditions were inferior compared to the first run and the median flux limit achieved was 2.7×10^{-18} erg s^{-1} cm^{-2} Å^{-1}. We observed 9 sources in total and detected an emission line in only one source. No continuum was detected in any other source either.

The flux limits reached during observations with the Hobby-Eberly Telescope are more variable, as the telescope tracking causes a variable illumination of the primary mirror resulting in varying noise levels. We find for our observations, which were taken across different seasons, 1σ noise levels ranging range from $2.0 - 7.0 \times 10^{-18}$ erg s^{-1} cm^{-2} Å^{-1}. On average, the blue channel is more sensitive compared to the red channel. The average flux limits reached during 6 different observations using Gemini North are 1.0×10^{-18} erg s^{-1} cm^{-2} Å^{-1}. The flux limits are also shown in Table 1.

2.3.2 Redshift determination and emission line measurements

After applying all the calibrations, the identification of emission lines in the extracted 1D spectra was attempted. The spectra of radio galaxies are dominated by one or several of the following emission lines: Lyα λ1216, [O II] λ3727, [O III] λ5007, Hα λ6563 + [N II] λ6583 and the initial redshift determination was based on the identification of one or more of these lines (McCarthy 1993; Röttgering et al. 1997; De Breuck et al. 2001). Relatively fainter lines such as C IV λ1549, He II λ1640, C III] λ1909, C II] λ2326 and Mg II λ2800

were then used in case of ambiguity arising from the identification of the stronger emission lines. For objects with a single emission line in the spectrum, we used the shape and the equivalent width of the emission line, in addition to near infrared magnitudes (where available) to identify the emission line for redshift determination. For example, an asymmetric line profile (combined with a faint near-infrared magnitude) would be a strong indicator of Lyα at high redshifts.

Once the redshift was determined we derived the integrated flux and full width at half maximum (FWHM), by fitting a single Gaussian to the emission line. In a few cases we detect double peaked emission lines (mostly Lyα λ1216 and [O II] λ3727), but for the purposes of this study we smoothed the spectrum in order to fit a single Gaussian to such lines. The above line identification methods yielded reliable redshifts for a total of 12 objects, which are presented in Table 3. Also shown are the flux densities and calculated radio luminosities at 150 MHz from Saxena et al. (2018a). The 1D spectra are shown in Figure A1 in Appendix A.

2.3.3 Notes on individual object spectra

(i) USS7, $z = 0.52$

Two emission lines, [O III] λ5007 and [O II] λ3727 at a redshift of $z = 0.52$ are detected in the spectrum. This source is slightly resolved in the radio image and the [O III] and [O II] line strengths suggest that this source is a faint high-excitation radio galaxy[5].

(ii) USS483, $z = 0.86$

This object has an interesting spectrum with only one bright emission line visible at 9291 . There is also faint continuum visible around the emission line, therefore ruling out the line identification as Lyα. We tentatively identify this line as [O III] λ5007, giving a redshift of $z = 0.86$. Hα is ruled out due to the absence of the expected [O III] line in this case. We do not detect [O II] λ3727 in the spectrum, which implies that this must be a HERG (Best & Heckman 2012).

The long-slit was aligned along the radio axis (Figure 2, top) and the line emission in the 2D spectrum (Figure 2, bottom) is extended along the radio axis, which implies interaction between the jet and the gas surrounding the host galaxy. The line emission can be seen extending up to 15 arcseconds, pointing towards the possibility of large scale emission line halos around the central radio galaxy.

(iii) USS43, $z = 1.46$

A redshift of $z = 1.46$ was confirmed using the [O II] λ3727 and Mg II λ2800 emission lines. Also detected in the spectrum is [Ne V] λ3426, which has been shown to be indicative of the presence of extended emission line regions (EELRs) due to the AGN in the host galaxy, which also contribute towards powering the [O II] emission in addition to star formation activity. (Maddox 2018). When applying a smoothing kernel to the spectrum, we also see faint C II] λ2324, C III] λ1909 and C IV λ1549 emission. C III] is blue-shifted by 30 , which is a better indicator of the systemic redshift of the

---

[5] High-excitation radio galaxies (HERGs) are a class of radio galaxies that show strong high-excitation emission lines. A characteristic feature of HERGs is their high [O III] equivalent widths (> 3) and high [O III]/[O II] ratios (see Best & Heckman 2012, for example).

Table 3. Details of detected emission lines, radio flux densities and luminosities at 150 MHz, and radio sizes of galaxies in this paper. The source IDs, radio flux densities and sizes are taken from Saxena et al. (2018a), which also gives the RA and Dec information for each source. We mention the telescope that was used to observe each source in the Tel. column. 'W' stands for William Herschel Telescope, 'G' for Gemini North and 'H' for Hobby-Eberly Telescope.

Source ID	z	Tel.	Line	Flux $(10^{-17}$ erg s^{-1} cm^{-2})	Luminosity $(10^{41}$ erg s^{-1})	FWHM (km s^{-1})	$S_{150\ \mathrm{MHz}}$ (mJy)	$\log L_{150\ \mathrm{MHz}}$ (W Hz^{-1})	LAS$_{\mathrm{rad}}$ (kpc)
USS7	0.52	W	[O II] $\lambda 3727$	4.5 ± 3.3	0.5 ± 0.3	970 ± 60	122 ± 24	26.2 ± 0.7	21.6 ± 0.6
			[O III] $\lambda 5007$	8.3 ± 2.1	0.9 ± 0.2	460 ± 30			
USS483	0.86	G	[O III] $\lambda 5007$	36.6 ± 1.7	13.0 ± 0.6	1050 ± 60	89 ± 16	26.4 ± 0.7	18.8 ± 0.8
USS43	1.46	W	Mg II $\lambda 2800$	5.0 ± 3.4	6.9 ± 4.7	640 ± 50	200 ± 40	27.6 ± 0.7	5.8 ± 0.8
			[O II] $\lambda 3727$	40.0 ± 3.0	55.0 ± 4.1	1380 ± 80			
USS182	2.02	H	Lyα	32.6 ± 5.0	96.5 ± 14.8	1420 ± 60	146 ± 30	27.8 ± 0.7	24.2 ± 0.8
USS18	2.06	H	Lyα	77.9 ± 4.3	242.0 ± 13.4	950 ± 60	131 ± 26	27.8 ± 0.7	9.5 ± 0.8
USS320	2.20	W, H, G	Lyα	8.7 ± 3.8	31.7 ± 13.9	1300 ± 100	86 ± 17	27.9 ± 0.7	19.6 ± 0.8
			Mg II $\lambda 2800$	3.2 ± 1.1	12.1 ± 4.1	320 ± 30			
USS268	2.35	W, H	Lyα	22.8 ± 2.8	97.6 ± 12.0	750 ± 50	92 ± 18	27.8 ± 0.7	12.6 ± 0.8
			Mg II $\lambda 2800$	5.2 ± 3.0	23.2 ± 13.4	320 ± 30			
USS98	2.61	W, G	Lyα	20.4 ± 1.6	112.7 ± 8.8	810 ± 30	178 ± 36	28.3 ± 0.7	56.9 ± 0.8
USS206	4.01	W	Lyα	19.5 ± 3.1	301.7 ± 50.0	1110 ± 200	102 ± 20	28.6 ± 0.7	58.7 ± 0.8
USS172	4.11	H	Lyα	5.2 ± 0.7	85.3 ± 11.5	570 ± 30	124 ± 25	28.6 ± 0.7	65.9 ± 0.7
USS188	4.57	H	Lyα	6.8 ± 0.7	143.3 ± 14.8	520 ± 20	166 ± 33	28.8 ± 0.7	26.2 ± 0.7
USS46	4.86	H	Lyα	5.1 ± 0.8	124.2 ± 20.0	500 ± 30	87 ± 17	28.7 ± 0.7	6.2 ± 0.6
USS202	5.72	G	Lyα	1.6 ± 0.6	57.0 ± 21.4	370 ± 30	170 ± 34	29.1 ± 0.7	6.3 ± 0.6
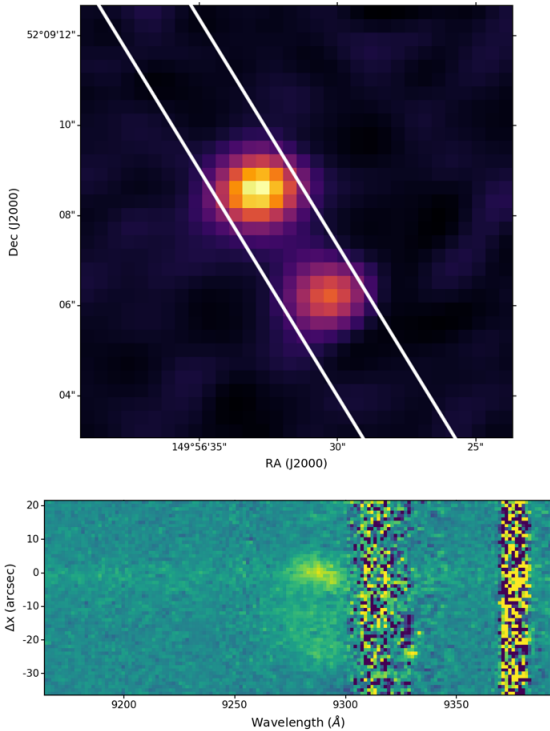
Figure 2. Top: VLA image of USS483 at 1.4 GHz, with a beam size of ∼ 1.3″. Also shown is the position of the GMOS long-slit, aligned along the radio axis. Bottom: The 2D line emission that we identify as [O III] at $z = 0.86$. The line emission is spatially extended along the radio axis, with emission extending all the way to ∼ 15″ away from the central host galaxy. This behaviour is a clear sign of interaction between the radio jet and the surrounding gas.

galaxy. However, since the signal-to-noise of this line is low, we quote the redshift measured using other lines instead. Our NIR imaging led to the detection of the host galaxy with $K = 21.6 \pm 0.2$ AB.

(iv) USS182, $z = 2.02$

A strong emission line that we identify as Lyα at $z = 2.02$ is detected in spectrum. No other lines or continuum are detected. The line is asymmetric, has an integrated flux of $32.6 \pm 5.0 \times 10^{-17}$ erg s^{-1} cm^{-2} and a broad FWHM of 1420 ± 60 km s^{-1}. Our NIR imagine led to the detection of the host galaxy with $K = 21.8 \pm 0.2$ AB.

(v) USS18, $z = 2.06$

A strong emission line, which we identify as Lyα at $z = 2.06$ is detected in the spectrum. The line also appears to be asymmetric, has a an integrated flux of $77.9 \pm 4.3 \times 1^{-17}$ erg s^{-1} cm^{-2} and a FWHM of 950 ± 60 km s^{-1}. No other lines or continuum are detected in the spectrum.

(vi) USS320, $z = 2.20$

The double-peaked Lyα emission line was identified at a redshift of $z = 2.20$. The Lyα emission seems to be extended in the 2D spectrum. There are also hints of very faint C IV, C II], Ne V and possible Mg II (although in sky lines) emission in the redder parts of the spectrum at the same redshift. We smooth the double-peaked Lyα emission line and fit with a single Gaussian, deriving a line flux of $8.7 \pm 3.8 \times 10^{-17}$ erg s^{-1} cm^{-2} and a FWHM of 1300 ± 100 km s^{-1}. The host galaxy is detected with a magnitude of $K = 21.7 \pm 0.3$ AB in our NIR imaging.

(vii) USS268, $z = 2.35$

We clearly detect a double peaked emission line, which we identify as Lyα at $z = 2.35$. Also detected in the redder parts of the spectrum is C II] and Mg II (although this is in sky lines) at the same redshift. We smooth the double peaked Lyα line and fit with a single Gaussian to calculate a line flux of $22.8 \pm 2.8 \times 10^{-17}$ erg s^{-1} cm^{-2} and FWHM of 750

± 50 km s^{-1}. Our NIR imaging led to the detection of the host galaxy with $J = 23.6 \pm 0.1$ AB and $K = 21.9 \pm 0.3$ AB.

(viii) USS98, $z = 2.61$

A single, strong Lyα emission line at a redshift of $z = 2.61$ is detected. The line appears to be asymmetric. There is no clear emission line in the redder parts, as most of the expected lines fall in regions with strong sky lines. Gaussian fit to the emission line gives a line flux of $20.4 \pm 1.6 \times 10^{-17}$ erg s^{-1} cm^{-2} and a relatively narrow FWHM of 810 ± 30 km s^{-1}.

(ix) USS206, $z = 4.01$

A single, bright and asymmetric emission line with possible multiple components is observed, which we identify as Lyα at $z = 4.01$. No other emission line is visible in the spectrum. No continuum is detected either. The measured line flux is $19.5 \pm 3.1 \times 10^{-17}$ erg s^{-1} cm^{-2}, with a broad FWHM of 1110 ± 200 km s^{-1}.

(x) USS172, $z = 4.11$

A single emission line is detected in the spectrum, which we identify with Lyα at $z = 4.11$. The line is faint, with an integrated flux of $5.2 \pm 3.0 \times 10^{-17}$ erg s^{-1} cm^{-2} and has a relatively narrow FWHM of 570 ± 30 km s^{-1}. No other emission line is detected in either the blue or the red channels of the spectrograph. The spatial extent of the Lyα emission is relatively compact, at 13.3×9.5 kpc. The host galaxy is detected in the NIR images with $J = 22.8 \pm 0.1$ AB and $K = 22.7 \pm 0.2$ AB.

(xi) USS188, $z = 4.57$

A single, weak emission line identified as Lyα at $z = 4.57$ is detected in the spectrum. The integrated line flux is $6.8 \pm 0.7 \times 10^{-17}$ erg s^{-1} cm^{-2} with a relatively narrow FWHM of 520 ± 20 km s^{-1}. NIR photometry of the host galaxy shows that it is undetected down to a 3σ depth of $J > 23.4$ AB, but is detected with $K = 21.6 \pm 0.2$ AB, where expected contamination from the [O II] $\lambda 3727$ emission line may be present.

(xii) USS43, $z = 4.86$

We detect a single, asymmetric emission line, which is identified as Lyα at $z = 4.86$ with an integrated flux of $5.1 \pm 0.8 \times 10^{-17}$ erg s^{-1} cm^{-2} and a narrow FWHM of 500 ± 30 km s^{-1}. This makes USS43 one of the highest redshift radio galaxies currently known. No other line is detected in the spectrum.

(xiii) USS202, $z = 5.72$

A single emission line, characteristic of Lyα at high redshift is detected in the spectrum of this object, giving a redshift of $z = 5.72$. This makes it the highest redshift radio galaxy observed to date. A detailed analysis of the emission line in this particular source is presented separately in Saxena et al. (2018b).

2.3.4 *Undetected sources*

There remain 10 USS sources that were targeted for spectroscopy and no emission lines were detected. From these, two sources have continuum detections but no emission lines, implying a possible low redshift. Rest of the sources could either lie in the redshift range where the bright optical emission lines are hard to observe from ground based telescopes ($1 < z < 2$), have passive galaxy type spectra lacking strong emission lines, or have very broad lines that were missed by our relatively shallow spectroscopy. The non-detections
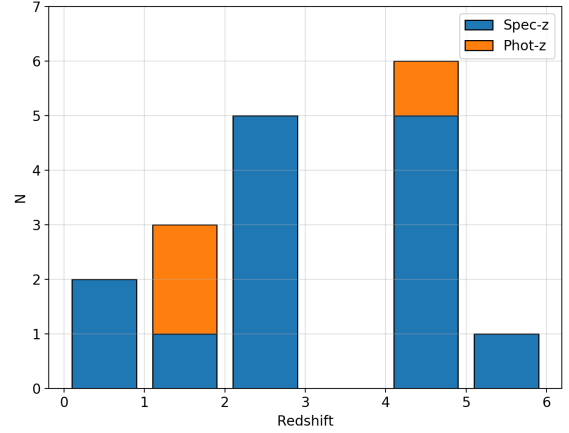
Figure 3. Stacked histogram of spectroscopic redshifts (blue) and photometric redshifts (orange) for radio sources in the Saxena et al. (2018a) sample. The total height of the bar shows the total number of objects with either spectroscopic or photometric redshifts in each bin. The distribution shows that the USS selection is effective at picking out high-redshift radio galaxies from a large area radio survey.

could also indicate that these sources are either (optically) faint, low mass radio galaxies, or lie at very high redshifts ($z > 6.5$).

2.4 **Properties of the faint radio galaxy sample**

2.4.1 *Redshift distribution*

In this section we look at the redshift distribution of the spectroscopically confirmed radio sources. Out of a total of 32 sources that were initially compiled by Saxena et al. (2018a), we spectroscopically confirmed redshifts for 12 of them. Figure 3 shows the distribution of these redshifts, along with photometric redshifts for three additional objects in the sample reported by Saxena et al. (2018a), which pushes the total number of sources with redshifts to 15. The spectroscopic redshift distribution peaks at $2 < z < 3$, with the total range of redshifts between $0.52 < z < 5.72$. This includes the recent discovery of the highest redshift radio galaxy discovered at $z = 5.72$, which was reported separately in Saxena et al. (2018b). The detection of a fair amount of $z > 2$ radio galaxies, through USS selection combined with optical faintness and compact radio sizes, is holds promise for similar studies in the future with even deeper radio surveys, such as the LOFAR Two-meter Sky Survey (Shimwell et al. 2017, 2019).

2.4.2 *Velocity dispersion*

For radio sources spectroscopically confirmed in this study, through [O II], [O III] and Mg II lines at low redshifts and the Lyα line at high redshifts ($z > 2$), the full width at half maximum (FWHM) of the emission lines is in the range $320 - 1420$ km s^{-1}. This range is lower than what is typically observed for much brighter radio galaxies across all redshifts (see De Breuck et al. 2000a, for example) and in the following

Table 4. Near infrared photometry for HzRGs and stellar mass measurements for radio galaxies in our sample.

Source ID	z	J (AB)	K (AB)	$\log M_\star$ ($M_\odot$)
USS43	1.46	–	21.6 ± 0.2	10.6 ± 0.4
USS182	2.02	–	21.8 ± 0.2	11.0 ± 0.4
USS320	2.20	–	21.7 ± 0.3	11.1 ± 0.4
USS268	2.35	23.6 ± 0.1	21.9 ± 0.3	11.1 ± 0.5
USS172	4.11	22.8 ± 0.1	22.7 ± 0.2	11.2 ± 0.5
USS188	4.57	> 23.4	$21.6 \pm 0.2^\star$	11.5 ± 0.5
USS202	5.72	> 25.3	> 24.2	< 10.5

*Expected contamination from [O II] $\lambda 3727$ emission line in the K band.

sections we compare the line widths with radio galaxies in the literature.

2.4.3   Stellar masses

We now estimate stellar masses for 8 (out of the 13 spectroscopically confirmed) new radio galaxies that were observed in K band. To do this, we first model the expected K band magnitudes for radio galaxies with different stellar masses across redshifts using the PYTHON package called SMPY (Duncan & Conselice 2015). SMPY is a stellar population modelling code designed for building composite stellar populations in an easy and flexible manner and allows for synthetic photometry to be produced for single or large suites of stellar population models. To build stellar populations, we use the Bruzual & Charlot (2003) model with a Chabrier (2003) initial mass function (IMF). We assume solar metallicity, similar to Willott et al. (2003), a formation redshift of $z_f = 25$ and a maximally old stellar population that has been forming stars at a constant rate. We follow the Calzetti et al. (2000) law for dust attenuation, using $A_v = 0.5$, in line with observations and predictions from McLure et al. (2018) and Cullen et al. (2018) at the redshifts and mass bins that are typical of radio galaxy hosts ($M_\star > 10^{10.2}\ M_\odot$). The synthetic photometry produced for stellar masses in range $10.6 < \log M_\star < 12.0$ is then convolved with the K band filter to calculate apparent K band magnitudes over a redshift range $0 < z < 7$. The individual stellar mass is determined by finding the best fit stellar mass track to the K band magnitude and redshift using chi-squared minimisation.

The NIR photometry for faint radio galaxies and stellar masses inferred from the models are shown in Table 4. The fainter radio galaxies have lower stellar masses on average when compared to the bright radio galaxies known in the literature. The $10^{12}\ M_\odot$ stellar mass limit predicted for radio galaxies by Rocca-Volmerange et al. (2004) stands even for our sample – there is no radio source with an inferred stellar mass higher than $10^{12}\ M_\odot$ in our sample. Overall, we find that fainter radio galaxies occupy the massive end of the stellar mass function at all redshifts, in line with previous observations that showed that radio galaxies are hosted by massive galaxies at every epoch (Rocca-Volmerange et al. 2004).

The highest redshift radio galaxy, TGSS J1530+1049 at $z = 5.72$, which was part of our sample and was presented in Saxena et al. (2018b) is one of the lowest stellar mass radio galaxy from our sample. It is important to remember, however, that the overall lower stellar masses of galaxies in our sample are obtained under the assumptions that go into the stellar population modelling mentioned earlier. The biggest uncertainty comes from the assumption of dust attenuation, $A_v = 0.15$. It may be possible that radio galaxy hosts are dustier, which would lead to a higher stellar mass than what we report. However, since our models are able to account for the scatter in the $K - z$ relation for known radio galaxies without requiring extremely large or extremely small stellar masses, the inferred stellar masses for galaxies in our sample seem to be in line with expectations. Broadband photometry across the full optical to mid-infrared wavelengths is required to put robust constraints on the physical properties of these radio galaxies.

3   COMPARISON WITH LITERATURE HZRG SAMPLE

In this section we compile a sample of known high-redshift radio galaxies ($z \geq 2$) from the literature to compare the sample of newly discovered faint HzRGs against. We begin by briefly describing the parent radio samples from which the literature $z > 2$ radio galaxies were selected. We particularly highlight the flux limits of each of these radio samples and note that a large majority of these radio samples have much higher flux density limits than the Saxena et al. (2018a) sample used in this study. We point the readers to the relevant references mentioned in the sample description for detailed information about the sources.

3.1   Literature samples

3.1.1   Röttgering et al. 1997

This sample contains spectroscopic follow-up of the Leiden ultra-steep spectrum (USS) sample (Röttgering et al. 1994) and the 4C USS sample Tielens et al. (1979). Röttgering et al. (1997) sample contains spectra for 64 radio galaxies, with 29 of them being at $z > 2$. Other Lyα properties from this sample are presented in van Ojik et al. (1997). The median radio flux density of these sources is in the range $1 - 2$ Jy.

3.1.2   De Breuck et al. 2001

This spectroscopic sample of radio galaxies follows up the USS radio sources that were first presented in De Breuck et al. (2000a). The De Breuck et al. (2001) sample contains spectra for 69 radio galaxies from the De Breuck et al. (2000a) radio sample and observations of a few other previously known HzRGs, with 22 of them confirmed at $z > 2$. The limiting radio flux density for various subsamples observed in this study ranges from $250 - 1000$ mJy.

3.1.3   Jarvis et al. 2001

This sample contains spectra for radio sources selected from the 6C* sample (Blundell et al. 1998). The Jarvis et al. (2001a) sample has a total of 29 spectra, 12 of which lie
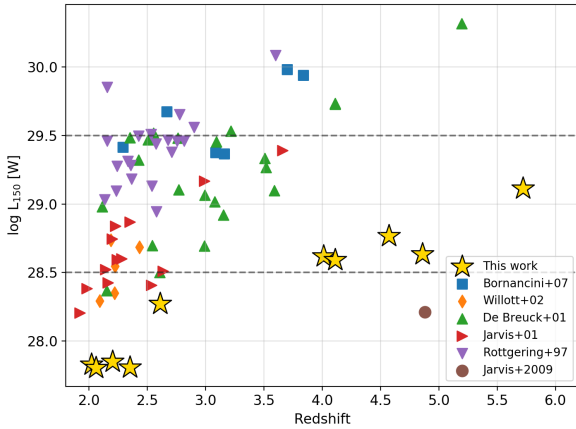
Figure 4. The distribution of radio luminosities and redshifts of the faint HzRGs (gold stars) and the literature galaxies (coloured symbols), which have been scaled to an observing frequency of 150 MHz. The faint HzRGs are almost an order of magnitude fainter at the highest redshifts, opening up a new parameter space for the discovery and study of radio galaxies in the early Universe.

at $z > 2$. The flux density at 151 MHz of sources in this sample is in the range $0.96 - 2$ Jy.

3.1.4 *Willott et al. 2002*

This sample contains optical spectroscopy for 49 radio sources selected from the 7C Redshift Survey, which is a spectroscopic survey of the regions covered in the 5C and 7C radio surveys. The Willott et al. (2002) sample contains 5 radio galaxies at $z > 2$. The radio flux density probed by this sample is $S_{151} > 0.5$ Jy.

3.1.5 *Bornacini et al. 2007*

This sample contains spectra for 14 USS sources selected from the Westerbork in the Southern Hemisphere (WISH) catalogue (De Breuck et al. 2002) and subsamples from the De Breuck et al. (2000a) USS catalogue. Six out of 14 sources observed by Bornancini et al. (2007) lie at $z > 2$. The limiting flux density of the WISH sample is $S_{352} \sim 18$ mJy.

3.1.6 *Radio luminosities*

The extended HzRG sample consists of a total of 75 radio galaxies at $z \geq 2$. All these radio galaxies have Lyα line measurements. We calculate the radio luminosities, radio sizes and Lyα luminosities for the literature HzRGs using the updated cosmology used in this study. Specifically for the radio luminosities at a frequency of 150 MHz, we use the published flux density at 150 MHz wherever available and when needed, we scale their flux density to 150 MHz using the published spectral index. For the newly spectroscopically confirmed radio galaxies reported in this paper, we use the radio measurements from Saxena et al. (2018a) to calculate radio luminosities.

The distribution of radio luminosities as a function of redshift is shown in Figure 4. Our sample of newly confirmed

faint HzRGs is marked with gold stars (and in all the following sections). It is immediately clear that our sample probes radio luminosities almost and order of magnitude fainter at the highest redshifts. This includes the discovery of the highest redshift radio galaxy known till date, TGSS J1530+1049 (Saxena et al. 2018b). We also show the faint radio galaxy detected by Jarvis et al. (2009), which was detected in a deep field and not from an all-sky survey, as an example of the kind of sensitivites that future radio surveys would be able to achieve to probe even fainter radio galaxies at high redshifts.

3.2 Comparison of emission line and radio properties

In this section we will explore how the emission line and radio properties of faint HzRGs compare with those of the literature HzRG sample.

3.2.1 *Lyα luminosities and FWHM*

We begin our analysis by first showing the distribution of Lyα line luminosities and FWHM values for faint HzRGs (gold stars) and literature HzRGs (black circles) across all redshifts in Figure 5. We note that the faint HzRGs in our sample show a systematically lower Lyα luminosity and FWHM compared to other HzRGs in the literature. The faint HzRG sample has a median Lyα luminosity of $\log L_{Ly\alpha} = 43.0$ erg s^{-1}, with 1σ standard deviation of 0.3 dex. The literature HzRG sample has a median Lyα luminosity of $\log L_{Ly\alpha} = 43.5$ erg s^{-1} but a much larger 1σ standard deviation of 0.7 dex. The difference in median FWHM values between the two samples is large, with faint HzRGs having median and standard deviation of 780 ± 340 (1σ) km s^{-1}, and the literature HzRGs having median and standard deviation of 1475 ± 800 km s^{-1}.

In Figure 6 we plot the Lyα luminosities with redshift for both faint and literature samples. The higher dispersion in the literature sample is seen across all redshifts, with a handful of sources at $z \sim 3 - 3.5$ showing significant deviations ($2.5-3\sigma$) from the median, such as WN J1053+5424 at $z = 3.1$ exhibiting the weakest Lyα luminosity of the sample ($\log L_{Ly\alpha} = 41.7$ erg s^{-1}) and TN J0205+2242 at $z = 3.5$ having the strongest luminosity ($\log L_{Ly\alpha} = 45.9$ erg s^{-1}). The faint HzRGs have comparable Lyα luminosities across redshifts. Overall, the luminosities (both faint and literature) do not seem to evolve much with redshift, with the Pearson's correlation coefficient $r = -0.02$ suggesting little to no evolution. Previously, Zirm et al. (2009) had reported the detection of lower luminosity Lyα emission from a sample of $z \sim 1$ radio galaxies that exhibited strong nebular emission lines, suggesting that the Lyα luminosities of extended halos around radio galaxies may undergo strong redshift evolution. Although our samples of both faint and literature radio galaxies do not exhibit very strong redshift evolution of Lyα luminosity, expanding the sample of faint radio galaxies at high redshifts may hold some clues about any such behaviour.

Next, we plot the Lyα line widths (FWHM) as a function of redshift for both faint and literature HzRG samples in Figure 7. We find a negative correlation between FWHM and
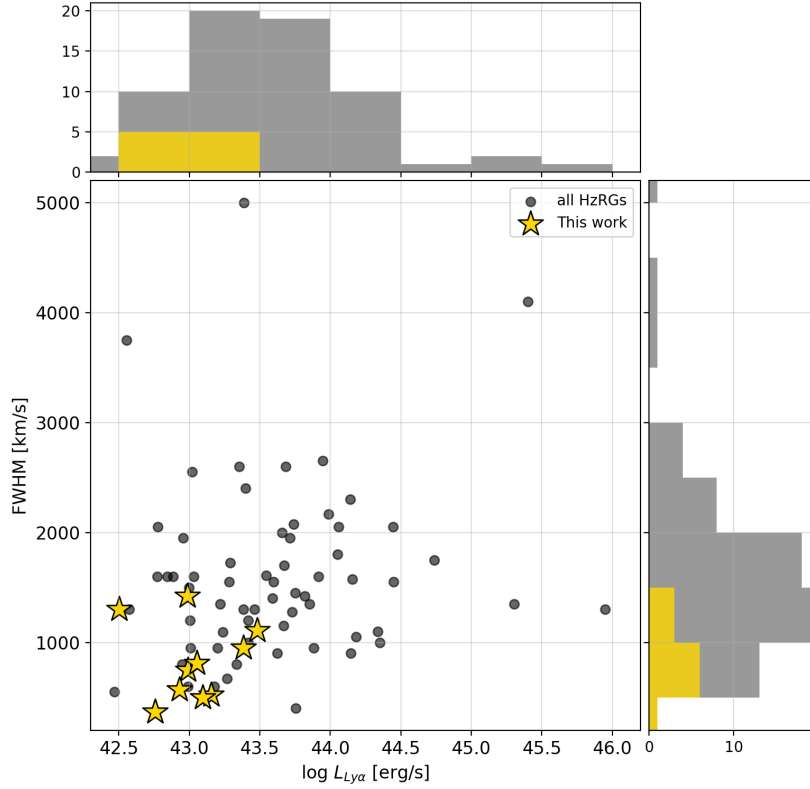
Figure 5. Distribution of Lyα luminosities and FWHM for faint (gold stars) and literature (black circles) radio galaxies. Also shown are the histograms of both these samples. Clearly, the faint HzRGs have lower Lyα luminosities and FWHM. In the text we give the median and standard deviations of Lyα luminosities and FWHM in the two samples. There is no correlation observed between the Lyα luminosities and FWHM for either of the two samples.
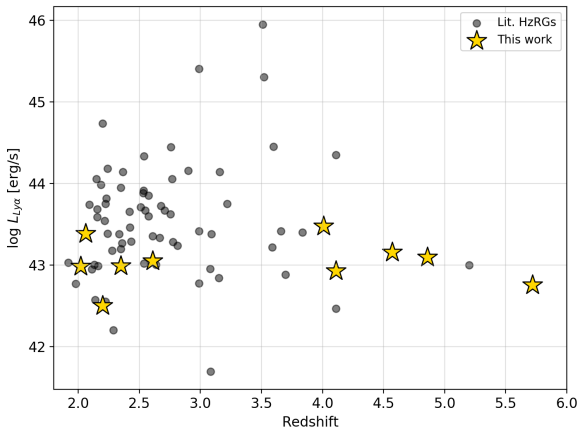

Figure 6. Lyα line luminosities as a function of redshift for the faint and literature HzRG samples. Across all redshifts, the faint HzRGs show lower luminosity values. We do not see any evolution in the line luminosity with redshift for either of the two HzRG samples.

redshift for both samples and the anti-correlation is stronger in the faint sample ($r = -0.77$, compared to $r = -0.12$ for the literature sample). From the literature sample, there are 3

radio galaxies at $z \sim 2 - 3$ that are 3σ outliers from the median value, with the radio galaxy 1113−178 from Röttgering et al. (1997) showing the broadest Lyα profile with FWHM = 5000 km s^{-1}.

3.2.2   Radio luminosity vs. Lyα luminosity

We now show Lyα line luminosities as a function of radio luminosity at 150 MHz for the faint and literature samples in Figure 8. We see a weak positive correlation in the literature sample, with $r = 0.06$, which is weaker than what Jarvis et al. (2001a) observed for their sample of radio galaxies. Conversely, in the faint HzRG sample we see a weak negative correlation, with $r = -0.08$. Both these r-values are consistent with little to no correlation between the two quantities, indicating that the radio luminosity (across several orders of magnitude) of a radio galaxy does not have much influence on its Lyα luminosity.

3.2.3   Linear sizes

In this section, we look at the linear size distribution of radio galaxies both samples. For faint HzRGs presented in this paper, we use the angular sizes reported by Saxena et al. (2018a). Linear sizes of literature HzRGs were calculated using the updated cosmology used in this study and their
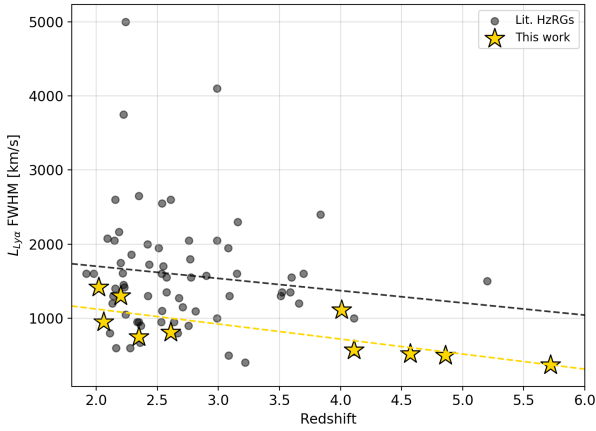
Figure 7. The Lyα FWHM as a function of redshift for the faint and literature HzRGs. Across all redshifts, faint HzRGs exhibit lower FWHM values when compared to the literature HzRGs. We see a decrease in FWHM with redshift in both samples, but the anticorrelation is stronger for faint HzRGs (orange dashed line) than the bright ones (black dashed line).

Figure 9. The distribution of radio luminosities at 150 MHz and linear sizes of sources in the faint and literature samples. the $P - D$ diagram tracks the evolution of radio sources through their lifetime. Clearly, The most luminous sources are able to grow out to larger sizes as their intrinsically more powerful jets work against the energy loss mechanisms that begin to dominate later in the radio source life. The faint HzRGs preferentially lie towards the low power, small size part of the plot, indicating that they must be young.

tracks essentially trace the evolutionary path that a radio source takes through its lifetime. For a given jet power, radio sources start out at the left side of the $P - D$ diagram. As radio sources grow, they lose energy, initially through adiabatic losses and at larger sizes due to inverse Compton losses because of interactions with the cosmic microwave background radiation (Kaiser & Best 2007). Overall, this results in the radio sources experiencing decreasing radio luminosities with increasing linear sizes, moving them towards the bottom-right side of the $P - D$ diagram. The $P - D$ tracks are influenced by magnetic field strength, redshift and the radio source environment.

As seen in Figure 9, the faint HzRGs lie in the part of the $P - D$ diagram corresponding to weaker and younger radio sources. We also note that the largest radio sources are also some of the most luminous ones and larger radio sources are expected to be older than the compact ones. Radio sources with intrinsically weaker jets are unable to grow out to large sizes as they are unable to overcome the increasing energy losses with increase in linear size, and are eventually extinguished before ever achieving large sizes (Saxena et al. 2017). This is evident from the lack of sources in the bottom-right part of the $P - D$ diagram. We discuss the redshift evolution of linear sizes of both the faint and literature samples in Section 4.4.

3.2.4 Radio spectral index vs. redshift

We now explore the observed correlation between the low-frequency radio spectral index (α) and redshift (z) in our extended HzRG sample in Figure 10. The $z - \alpha$ correlation for radio galaxies has often been used to identify HzRG candidates in large area radio surveys (see Röttgering et al. 1997, for example).

Figure 8. Lyα luminosities as a function of radio luminosity at 150 MHz for faint and literature HzRGs. There is a positive correlation observed between the two quantities for literature HzRGs, however it is weaker than what some previous studies have found. However, we do not see any correlation between the two for faint HzRGs.

published angular sizes. The median size of our faint radio sources is 22 kpc and the median size of the literature HzRGs is 42 kpc. It is important to remember that Saxena et al. (2018b) introduced an angular size restriction ($< 10''$) while selecting faint HzRG candidates, which would preferentially select compact radio sources across all redshifts.

We show the distribution of radio luminosities at 150 MHz as a function of linear size for both the faint and the literature HzRGs in Figure 9. These so-called '$P-D$' diagrams have long been used to characterise the growth and evolution of powerful radio sources across all redshifts (Kaiser et al. 1997; Blundell et al. 1999; Saxena et al. 2017). The $P - D$
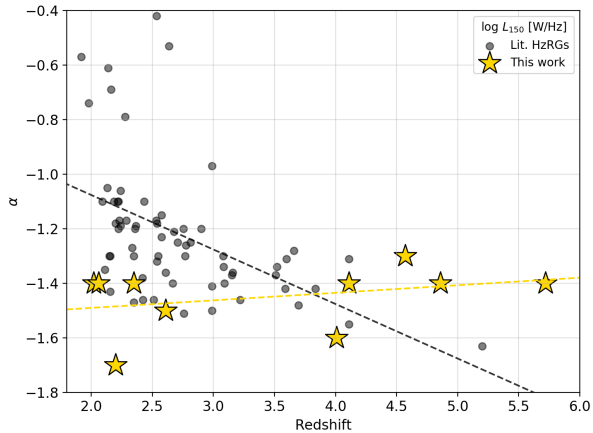
Figure 10. Low-frequency radio spectral index as a function of redshift for both faint and literature HzRGs. We observe an anti-correlation between z and α for the literature sample, which has been used successfully to select promising HzRG candidates from large radio surveys. However, the faint HzRGs actually show a positive correlation between the two. Since most of the HzRGs presented in this study were initially selected because of their spectra, the observed correlations are likely to contain several biases.

We observe an anti-correlation between redshift and spectral index in the radio galaxies from the literature, with $r = -0.50$. However, it is important to note that most of the radio galaxies that are part of the extended sample were initially selected because of their ultra-steep spectra (USS) at low radio frequencies ($\alpha < -1$), which bias the distribution and lead to the recovered correlation. From our sample of faint galaxies, which were also selected for having ultra-steep spectra, we do not see a strong anti-correlation between spectral index and redshift. In fact, the faint radio galaxies exhibit a positive correlation between α and z, in contrast to what is seen for literature HzRGs. Further, we do not find extremely steep spectral indices at the highest redshifts, even though the best-fit from the literature would suggest so.

The origin of the observed $z - \alpha$ correlation was investigated by Morabito & Harwood (2018), where they found that a combination of inverse Compton losses at high redshifts and selection effects were able to explain the observed $z - \alpha$ correlation in radio galaxies. Inverse Compton losses affect the high frequency parts of the radio SED, which results in an overall steeper spectral index when measured at low-frequencies. Inverse Compton losses are also expected to affect the linear sizes of radio sources. However, we do not find any strong correlation between the spectral index and linear sizes of radio sources in either of the two samples studied.

4 DISCUSSION

4.1 Lyα emission in faint HzRGs is powered by weak AGN

As shown in Figure 5, our newly discovered faint radio galaxies have lower Lyα luminosities and FWHM values across all redshifts compared to the bright HzRGs known in the literature. The dispersion in their Lyα luminosities is also lower. This is interesting because the distribution of Lyα luminosities and FWHM for brighter HzRGs shows a much larger variety (3σ dispersion of log $L_{Ly\alpha} = 2.1$ erg s^{-1}, as opposed to 0.6 erg s^{-1} for the faint radio galaxies, as shown in Section 3.2.1). Historically, the large luminosities and equivalent widths of Lyα emission from bright HzRGs have been explained by anisotropic photoionisation from an obscured AGN in combination with jet-induced shock ionisation or contribution from hot stars (Chambers et al. 1990; Baum et al. 1992; McCarthy 1993; van Ojik et al. 1996, 1997; De Breuck et al. 2000b). Additionally, physical phenomena such as launching of winds and outflows from the central AGN (see Nesvadba et al. 2008, for example), bursts of star formation and radio AGN activity driven by recent mergers (see Villar-Martín et al. 2007b, for example) and gas infall on to the host galaxy (see Villar-Martín et al. 2007a, for example) are sometimes required to explain the UV line ratios and large velocity dispersions at high redshifts.

The systematically lower Lyα luminosities in faint HzRGs indicate that the line emission must be ionised by a weaker AGN, or by modest star-burst activity. To accurately disentangle the relative contributions from AGN and star-formation, rest-frame optical nebular emission lines are needed to then use the BPT diagram (Baldwin et al. 1981). Lyα alone can not be used to make clear distinctions between the underlying ionising sources, and other faint UV lines will be vital in disentangling the contribution from various sources of ionisation within the host galaxies.

4.2 No direct evidence of strong interaction between radio jet and line-emitting gas

Another indication of the absence of shocks is the lack of evidence for strong jet-gas interaction – we do not see an anti-correlation between Lyα FWHM and linear size, which has previously been interpreted as a signature of jet-gas interaction in radio galaxies (van Ojik et al. 1997; Baum & McCarthy 2000; Best et al. 2000). The origin of this anti-correlation has been attributed to jets in smaller radio sources still being in the process of propagating through the relatively dense interstellar medium of their host galaxies, which leads to transfer of kinetic energy from the jets to the line emitting gas, resulting in larger line widths (see van Ojik et al. 1997, for example). For larger radio sources, when the jet has passed well beyond the emission line regions, the emission line widths are narrower indicating that the gas has more relaxed and settled kinematics.

In fact, when combining the faint and literature HzRG samples, it is clear that even though some of the largest radio sources in our sample show narrower Lyα line widths, we can not conclusively infer that narrow line widths are a consequence of less jet-gas interaction, as shown in Figure 11 in which the faint HzRGs are marked with gold stars
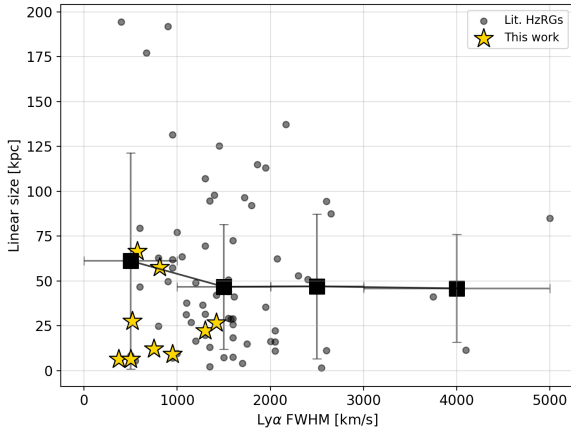
Figure 11. The linear sizes of faint HzRGs (gold stars) are not seen to anti-correlate with Lyα FWHM, which is indicative of absence of strong jet-gas interaction. This implies that shocks do not play a strong role in powering the Lyα emission in faint HzRGs. The anti-correlation in the combined sample of faint and literature HzRGs, calculated by binning in FWHM, is also very weak (black squares), although we see that the largest literature HzRGS often also exhibit narrower FWHM.

and literature HzRGs with black circles. The median linear sizes in the combined sample were calculated in bins of Lyα FWHM. These FWHM bins are $0 - 1000$, $1000 - 2000$, $2000 - 3000$ and > 3000 km s^{-1}. Therefore, from our data we can not conclusively pin-point the dominant impact of jet-gas interactions in smaller radio sources. However, the added complexity of probing radio sources across a broad range of radio and Lyα luminosities as well as redshifts in our sample may dilute out any strong effects that may be seen in subsets of relatively similar radio galaxies.

4.3 Faint HzRGs have lower stellar masses

As shown earlier, the apparent K-band magnitudes for a subset of faint radio galaxies presented in this paper were lower than what has been observed for more powerful radio sources across all redshifts. Using simple stellar population modelling, we find that the stellar masses inferred for faint HzRGs are also lower than what has been typically determined for bright HzRGs (see Rocca-Volmerange et al. 2004, for example). This is shown in Figure 12, where we show apparent magnitudes for our faint HzRGs along with those from HzRGs in the literature.

Also shown are predictions for apparent K magnitude from our stellar population synthesis modelling. Our faint HzRGs lie closer to the lower mass tracks, with the exception of USS188 with a stellar mass of $M_\star = 10^{11.7\pm0.7}$ $M_\odot$. However, contamination from the [O II] $\lambda3727$ emission line is expected in the K band and it is therefore likely that the stellar mass for this galaxy is being overestimated. The stellar mass estimates presented in this paper are based on only the K band magnitudes and photometry in additional bands and more detailed stellar population modelling is required to accurately measure stellar masses for our sample of faint HzRGs.
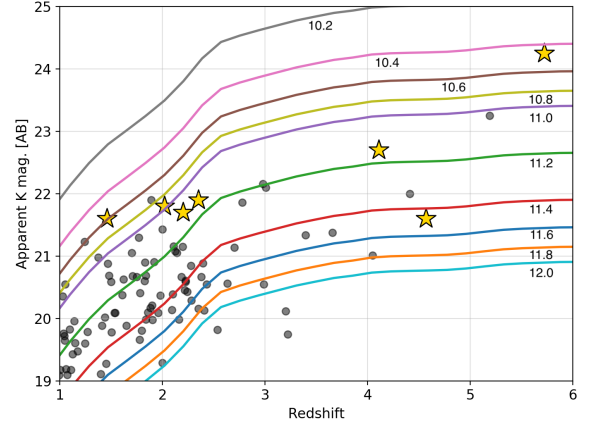
Figure 12. Apparent K band magnitudes and redshifts for faint HzRGs (gold stars) and those from the literature (black dots). The solid lines indicate photometry obtained using simple stellar population modelling as described in Section 2.4.3. We indicate the $\log M_\star$ ($M_\odot$) corresponding to each solid line on the plot. Our fainter radio galaxies have lower stellar masses when compared to the previously known, more powerful radio galaxies across all redshifts. We note that TGSS J1530+1049 at $z = 5.72$ has only a stellar mass limit, as it was undetected in our NIR imaging campaign (Saxena et al. 2018b). The galaxy with the brightest K mag in our sample (USS188 at $z = 4.57$) has expected contamination from the [O II] emission line in the broad band, which probably leads to an overestimated stellar mass using simple models.

4.4 The nature of faint HzRG hosts

As shown earlier, the faint HzRGs reported in this paper overall show weaker Lyα luminosities and narrower line widths in comparison to the brighter HzRGs. These fainter radio galaxies are also less massive than the brighter ones. Questions naturally arise about the nature of faint radio galaxies at high redshifts. In this section we attempt to provide some qualitative constraints on this.

To understand the nature of fainter radio galaxies, we compare their Lyα line luminosities and widths with bright, 'non-radio' Lyα emitters (LAEs) at comparable redshifts from the literature. In this analysis, we include the 21 LAEs observed by Sobral et al. (2018) in the redshift range $z \sim 2-3$, which were initially selected from narrow-band surveys and then followed up spectroscopically. Sobral et al. (2018) identify three broad classes of objects in their sample – broad-line AGN, narrow-line AGN and star-forming galaxies. We also include the sample of 18 LAEs in the redshift range $z \sim 3 - 5$ observed by Saito et al. (2008). This sample is divided into low EW (< 200 Å) and high EW (> 200 Å) sources and both subsamples contain star-forming galaxies.

In Figure 13 we show the Lyα luminosities and FWHM for the faint HzRGs (gold stars), the literature HzRG sample (black dots), and the LAEs from Sobral et al. (2018) (squares) and Saito et al. (2008) (diamonds). Clearly, the literature HzRGs show a large scatter in both Lyα luminosity and FWHM values, whereas the distribution for faint HzRGs has a lower scatter. The faint HzRGs overlap with SF galaxies and narrow-line AGN, but not broad-line AGN, whereas a large number of literature radio galaxies occupy

the same parameter space as broad-line AGN. Another interesting trend is the tight distribution in the parameter space of star-forming galaxies in both Sobral et al. (2018) and Saito et al. (2008) samples, and 8 of our faint radio galaxies follow this trend all the way into the parameter space occupied by AGN. Four galaxies from our sample with FWHM < 600 km s^{-1}(below the dashed horizontal line), which all also are at $z > 4$, show a complete overlap with star-forming galaxies from both LAE samples. We now try and qualitatively describe the nature of radio galaxy hosts, based on what was inferred for the bright 'non-radio' LAEs that we use for comparison.

4.4.1   Faint HzRGs at $z \sim 2 - 4$

We first look at the fainter HzRGs presented in the redshift range $z \sim 2 - 4$. This range consists of 6 out of the 10 sources at $z > 2$ with Lyα measurements (lying above the dashed black line). We note that these radio galaxies occupy the regions in the parameter space in Figure 13 that mark the transition between the star-forming and AGN populations. For these, the Sobral et al. (2018) galaxies offer a good sample for comparison owing to their comparable redshift range. We note that for their bright LAEs, Sobral et al. (2018) use photoionisation modelling to show that the star-forming galaxies (green squares) have a starburst age of ~ 20 Myrs, ionisation parameters $\log U \sim -3$ and mildly sub-solar gas metallicities. For AGN, they find an ionisation parameter $\log U \sim 0.6$ and higher gas metallicities, extending up to $2Z_\odot$.

Since two or more UV emission lines are essential to accurately determine the dominant source of ionisation, and as we only detect a single Lyα line in a majority of our shallow spectra, we must rely on inferring ionisation properties by qualitative comparison alone. Following the measurements of Sobral et al. (2018), we can conclude that faint radio galaxies at $z \sim 2 - 4$ represent a population that is transitioning from being AGN dominated to star-formation dominated. This is in contrast to a majority of bright radio galaxies known in the literature at these redshifts that display AGN-like features (see De Breuck et al. 2001, for example). Further, we do not see any source that could be classified as a broad-line AGN. Therefore, faint radio galaxies in this redshift range must either be recent starbursts or narrow-line AGN, or a population transitioning from one to the other. Very little is known about faint radio galaxies at these redshifts and larger samples combined with deeper spectroscopy are essential to understand the nature of such sources.

4.4.2   Faint HzRGs at $z > 4$

We now look at the 4 radio galaxies (lying below the black dashed line in Figure 13) that completely overlap with the star-forming LAE population. Perhaps a more direct comparison in terms of redshift for these is offered by the Saito et al. (2008) sources. The low EW LAEs in the Saito et al. (2008) sample have been identified as moderate starbursts, with star formation rates in the range $3.3 - 13$ $M_\odot$ yr^{-1}. The presence of weak AGN in these sources can not be completely ruled out. For the high EW LAEs, Saito et al. (2008)

rule out the presence of 'superwinds' launched by bursts of star formation or ionisation by a central AGN as the dominant ionising mechanism. Owing to the observed tight correlation between the line luminosities and widths, Saito et al. (2008) conclude that the origin of line emission in high EW LAEs is most likely due to accretion of cold gas on to the galaxy, placing them in an early phase of their evolution.

We may conclude that since our $z > 4$ radio galaxies coincide well with the distribution of both low and high EW LAEs, they are likely to be powered either by ordinary starbursts or by cold accretion. Both Saito et al. (2008) and Sobral et al. (2018) sources lying in this parameter space do not favour AGN as the dominant ionising source. Therefore, we can say with some confidence that faint radio galaxies at $z > 4$ in our sample are starburst dominated, which is different from what has been previously observed in brighter radio galaxies at these redshifts. Further, our radio galaxies show a positive correlation and a tight distribution between Lyα luminosity and line width, in line with the trend observed by Saito et al. (2008). Therefore, we may also infer that faint HzRGs at $z > 4$, if powered by cold accretion, are in an early stage of their evolution and are actively building up their stellar masses. This is consistent with the lower than average stellar masses calculated for these radio galaxies.

The suggestion that faint radio galaxies at $z > 4$ are actively building up their stellar mass is not entirely implausible, since radio sources at the highest redshifts are expected to be young (see Blundell et al. 1999, for example). Recent VLBI radio observation of TGSS J1530+1049, a radio galaxy from our sample at $z = 5.72$ (Saxena et al. 2018b), by Gabányi et al. (2018) revealed two distinct lobes separated by only $0.4''$, confirming that the radio source is young and that the host galaxy must also be in a very early phase of its evolution.

We highlight a caveat of shallow spectroscopy though, which is possibly missing out on sources with broad emission lines. Broad lines may be present in the spectra of sources that we did not detect in our spectroscopy using relatively short exposure times, and observations of these possible broad lines may alter the inferred physical properties of faint radio galaxies that have been reported in this section.

4.5   Inverse Compton losses dominant at high redshift

Although there is no strong redshift evolution seen in the sizes of the faint HzRGs reported in this paper, we do observe an evolution of radio sizes with redshift of literature radio galaxies. To gain better insights into the overall redshift evolution at $z > 2$, we combine the new faint and literature samples and bin the sources in redshift bins of $z < 2.5$, $2.5 - 3.0$, $3.0 - 3.5$, $3.5 - 4.0$, $4.0 - 5.0$ and $5.0 - 6.0$. The median linear sizes in each redshift bin as a function of redshift are shown in Figure 14. The error bars on the y axis indicate the 1σ standard deviations in the redshift bins. In the highest redshift bin only two sources are present and therefore the small error bar is only indicative of ΔLAS.

The strong evolution of radio sizes and the size distribution of individual sources are consistent with the prediction for the evolution of radio sizes with redshift from Saxena et al. (2017), where the decrease in radio size at
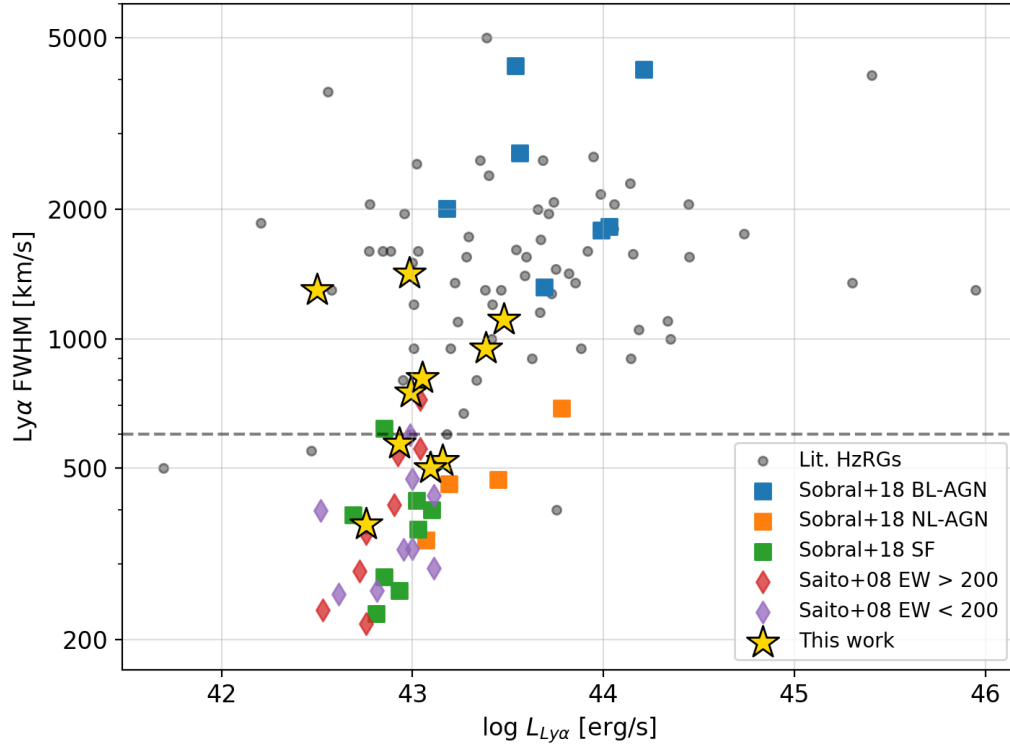
Figure 13. Lyα luminosity plotted against line width for faint (gold stars) and literature (black circles) HzRGs. Also shown are 'non-radio' Lyα emitting galaxies (LAEs) from Sobral et al. (2018) in the redshift range $z \sim 2 - 3$, consisting of star-forming galaxies (green squares), narrow-line AGN (orange squares) and broad-line AGN (blue squares). We also show LAEs observed by Saito et al. (2008) in the redshift range $z \sim 3 - 5$, divided into low EW (< 200 Å; purple diamonds) and high EW(> 250 Å; red diamonds). The black dashed line at FWHM $= 600$ km s^{-1} divides the faint radio galaxies at $z \sim 2 - 4$ (lying above) and $z > 4$ (lying below). We find that $z \sim 2 - 4$ radio galaxies form a bridge between the star-forming and narrow-line AGN populations, whereas the $z > 4$ radio galaxies overlap fully with the star-forming galaxy population. Our $z > 4$ sources are likely powered by either moderate starburst activity or cold accretion, and must be actively building up their stellar mass.

high redshifts is primarily dominated by inverse Compton (IC) losses. This suggests that IC scattering is the dominant energy loss mechanism at high redshifts. The enhanced IC losses, due to an increasing energy density of the cosmic microwave background radiation at high redshifts, dominate over other energy loss mechanisms such as synchrotron or adiabatic losses (see Saxena et al. 2017, for example).

5 SUMMARY

In this section we summarise the key findings of this paper. We have obtained spectroscopic redshifts for 13 out of the 32 sources that were selected for having an ultra-steep radio spectral index in the Saxena et al. (2018a) sample. These radio galaxies are almost an order of magnitude fainter than those that were previously discovered from large-area radio surveys and probe a new parameter space in low radio frequency flux densities. In addition to spectroscopy we have also obtained deep near-infrared imaging for a subset of the confirmed radio galaxies.

Next, we have compiled a sample of known $z > 2$ radio galaxies in the literature that have Lyα measurements.

The literature HzRG sample was then used to compare the properties of our faint radio galaxies across redshifts. We explored the radio and optical properties of the both the faint and literature high-redshift radio galaxies The main conclusions of this study are as follows:

(i) The newly confirmed fainter radio galaxies lie in the redshift range $0.52 \leq z \leq 5.72$, including the discovery of the highest redshift radio galaxy discovered to date, TGSS J1530+1049, which was first reported in Saxena et al. (2018b). The Lyα emission line profiles show a wide variety of FWHM values, ranging from $320 - 1240$ km s^{-1}. The Lyα luminosities and FWHM are systematically lower than what has previously been observed for brighter radio galaxies at these redshifts. Due to fainter line luminosities, narrower line widths and no evidence of ionisation by shocks in the faint HzRGs, we conclude that Lyα emission in these galaxies must be powered by weak AGN.

(ii) We use K band photometry for a subset of spectroscopically confirmed faint HzRGs presented in this paper to estimate stellar masses. Simple stellar population synthesis models are used for this. We find that the stellar masses to lie in the range $10.7 < \log M_\star < 11.7$ $M_\odot$, which are lower than
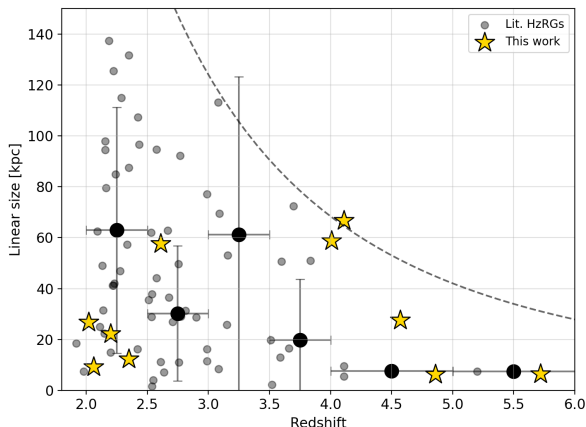
Figure 14. Linear sizes of HzRGs the faint (gold stars) and literature (black circles) samples with redshift. The median sizes, which are calculated by binning all radio sources in the combined HzRG sample in redshift bins, are shown as large black circles. Also shown are the predictions for redshift evolution of linear sizes due to inverse Compton losses, through interaction with the ambient cosmic microwave background radiation, from Saxena et al. (2017), that effectively provide an upper limit on achievable radio size. The median sizes of radio sources evolve strongly with redshift, and are well described by the Saxena et al. (2017) prediction, indicating that the dominant energy loss mechanism that shapes the size distribution of radio sources at high redshifts are inverse Compton losses.

what is seen for brighter HzRGs in the literature. Therefore, fainter HzRGs are hosted by galaxies with lower stellar masses, which are in a phase of building up their stellar mass rapidly.

(iii) We do not find any strong evidence for the presence of shocks in our sample of faint HzRGs. Therefore, we conclude that the dominant sources of ionisation in faint HzRGs must either be weak AGN or star-formation. We compare the Lyα line luminosity and width with strong, 'non-radio' Lyα emitting galaxie and find that faint HzRGs in the redshift range $z \sim 2-4$ form a bridge between the star-forming and narrow-line AGN populations. They do not show broad-line AGN characteristics. At $z > 4$, faint HzRGs completely overlap with the star-forming galaxy population, from which we infer that they must be powered either by moderate or intense star-burst activity. It is also possible that $z > 4$ radio galaxies are powered by cold accretion, which in combination with their low stellar masses shows that they must be in the process of assembling their stellar mass.

(iv) The linear sizes of faint HzRGs do not evolve much with redshift, but the sizes of the literature HzRGs exhibit a decrease with increasing redshift. We find that the redshift evolution of sizes of sources in a combined sample of faint and literature HzRGs matches well with predictions of size evolution due to increased inverse Compton losses at high redshifts. Therefore, the dominant energy loss mechanism in radio galaxies at high redshifts is the energy loss due to interactions with the cosmic microwave background radiation, and not synchrotron or adiabatic losses.

There remain many radio sources from the original Sax-

ena et al. (2018a) sample that still do not have a spectroscopic redshift and are high-priority targets for spectroscopy. Our new sample of HzRGs, that probes fainter flux densities over a large area on the sky, has offered glimpses into the nature of relatively less powerful radio galaxies at high redshifts. Ongoing large area surveys that are even more sensitive at low radio frequencies, such as the LOFAR Two-Meter Sky Survey (Shimwell et al. 2017, 2019) will uncover many more faint radio galaxies at high-redshifts, furthering our understanding of how radio galaxies are fuelled and their impact on their surroundings.

REFERENCES

Afonso J., et al., 2011, ApJ, 743, 122

Alam S., et al., 2015, ApJS, 219, 12

Archibald E. N., Dunlop J. S., Hughes D. H., Rawlings S., Eales S. A., Ivison R. J., 2001, MNRAS, 323, 417

Astropy Collaboration et al., 2013, A&A, 558, A33

Baldwin J. A., Phillips M. M., Terlevich R., 1981, PASP, 93, 5

Baum S. A., McCarthy P. J., 2000, AJ, 119, 2634

Baum S. A., Heckman T. M., van Breugel W., 1992, ApJ, 389, 208

Becker R. H., White R. L., Helfand D. J., 1995, ApJ, 450, 559

Best P. N., Heckman T. M., 2012, MNRAS, 421, 1569

Best P. N., Longair M. S., Röttgering H. J. A., 1998a, MNRAS, 295, 549

Best P. N., et al., 1998b, MNRAS, 301, L15

Best P. N., Röttgering H. J. A., Longair M. S., 2000, MNRAS, 311, 23

Blundell K. M., Rawlings S., Eales S. A., Taylor G. B., Bradley A. D., 1998, MNRAS, 295, 265

Blundell K. M., Rawlings S., Willott C. J., 1999, AJ, 117, 677

Bornancini C. G., De Breuck C., de Vries W., Croft S., van Breugel W., Röttgering H., Minniti D., 2007, MNRAS, 378, 551

Bruzual G., Charlot S., 2003, MNRAS, 344, 1000

Calzetti D., Armus L., Bohlin R. C., Kinney A. L., Koornneef J., Storchi-Bergmann T., 2000, ApJ, 533, 682

Carilli C. L., Harris D. E., Pentericci L., Röttgering H. J. A., Miley G. K., Kurk J. D., van Breugel W., 2002, ApJ, 567, 781

Chabrier G., 2003, PASP, 115, 763

Chambers K. C., Miley G. K., van Breugel W. J. M., 1990, ApJ, 363, 21

Chambers K. C., Miley G. K., van Breugel W. J. M., Huang J.-S., 1996, ApJS, 106, 215

Chambers K. C., et al., 2016, preprint, (arXiv:1612.05560)

Cullen F., et al., 2018, MNRAS, 476, 3218

De Breuck C., van Breugel W., Röttgering H. J. A., Miley G., 2000a, A&AS, 143, 303

De Breuck C., Röttgering H., Miley G., van Breugel W., Best P., 2000b, A&A, 362, 519

De Breuck C., et al., 2001, AJ, 121, 1241

De Breuck C., Tang Y., de Bruyn A. G., Röttgering H., van Breugel W., 2002, A&A, 394, 59

De Breuck C., et al., 2010, ApJ, 725, 36

Dewdney P. E., Hall P. J., Schilizzi R. T., Lazio T. J. L. W., 2009, IEEE Proceedings, 97, 1482

Duncan K., Conselice C. J., 2015, MNRAS, 451, 2030

Emonts B. H. C., et al., 2014, MNRAS, 438, 2898

Gabányi K. É., Frey S., Gurvits L. I., Paragi Z., Perger K., 2018, Research Notes of the American Astronomical Society, 2, 200

Garzon F., et al., 2004, in Moorwood A. F. M., Iye M., eds, Proc. SPIE Vol. 5492, Ground-based Instrumentation for Astronomy. pp 1187–1195, doi:10.1117/12.550961

Hatch N. A., et al., 2011, MNRAS, 410, 1537

Hook I. M., Jørgensen I., Allington-Smith J. R., Davies R. L., Metcalfe N., Murowinski R. G., Crampton D., 2004, PASP, 116, 425

Hunter J. D., 2007, Computing In Science & Engineering, 9, 90

Ishwara-Chandra C. H., Sirothia S. K., Wadadekar Y., Pal S., Windhorst R., 2010, MNRAS, 405, 436

Jannuzi B. T., Elston R., Schmidt G. D., Smith P. S., Stockman H. S., 1995, ApJ, 454, L111

Jarvis M. J., et al., 2001a, MNRAS, 326, 1563

Jarvis M. J., Rawlings S., Eales S., Blundell K. M., Bunker A. J., Croft S., McLure R. J., Willott C. J., 2001b, MNRAS, 326, 1585

Jarvis M. J., Teimourian H., Simpson C., Smith D. J. B., Rawlings S., Bonfield D., 2009, MNRAS, 398, L83

Kaiser C. R., Best P. N., 2007, MNRAS, 381, 1548

Kaiser C. R., Dennett-Thorpe J., Alexander P., 1997, MNRAS, 292, 723

Ker L. M., Best P. N., Rigby E. E., Röttgering H. J. A., Gendre M. A., 2012, MNRAS, 420, 2644

Lawrence A., et al., 2007, MNRAS, 379, 1599

Lee H., Chonis T. S., Hill G. J., DePoy D. L., Marshall J. L., Vattiat B., 2010, in Ground-based and Airborne Instrumentation for Astronomy III. p. 77357H, doi:10.1117/12.857201

Maddox N., 2018, MNRAS, 480, 5203

McCarthy P. J., 1993, ARA&A, 31, 639

McCarthy P. J., Baum S. A., Spinrad H., 1996, ApJS, 106, 281

McLure R. J., Willott C. J., Jarvis M. J., Rawlings S., Hill G. J., Mitchell E., Dunlop J. S., Wold M., 2004, MNRAS, 351, 347

McLure R. J., et al., 2018, MNRAS, 476, 3991

Miley G., De Breuck C., 2008, A&ARv, 15, 67

Miley G. K., Chambers K. C., van Breugel W. J. M., Macchetto F., 1992, ApJ, 401, L69

Miley G. K., et al., 2004, Nature, 427, 47

Miley G. K., et al., 2006, ApJ, 650, L29

Morabito L. K., Harwood J. J., 2018, MNRAS, 480, 2726

Nesvadba N. P. H., Lehnert M. D., De Breuck C., Gilbert A. M., van Breugel W., 2008, A&A, 491, 407

Orsi Á. A., Fanidakis N., Lacey C. G., Baugh C. M., 2016, MNRAS, 456, 3827

Pentericci L., et al., 2000, A&A, 361, L25

Pérez F., Granger B. E., 2007, Computing in Science and Engineering, 9, 21

Rawlings S., Eales S., Lacy M., 2001, MNRAS, 322, 523

Reuland M., Röttgering H., van Breugel W., De Breuck C., 2004, MNRAS, 353, 377

Rigby E. E., Best P. N., Brookes M. H., Peacock J. A., Dunlop J. S., Röttgering H. J. A., Wall J. V., Ker L., 2011, MNRAS, 416, 1900

Robinson A., Binette L., Fosbury R. A. E., Tadhunter C. N., 1987, MNRAS, 227, 97

Robitaille T., Bressert E., 2012, APLpy: Astronomical Plotting Library in Python, Astrophysics Source Code Library (ascl:1208.017)

Rocca-Volmerange B., Le Borgne D., De Breuck C., Fioc M., Moy E., 2004, A&A, 415, 931

Röttgering H. J. A., Lacy M., Miley G. K., Chambers K. C., Saunders R., 1994, A&AS, 108, 79

Röttgering H. J. A., van Ojik R., Miley G. K., Chambers K. C., van Breugel W. J. M., de Koff S., 1997, A&A, 326, 505

Röttgering H., Daddi E., Overzier R., Wilman R., 2003, New Astron. Rev., 47, 309

Saito T., Shimasaku K., Okamura S., Ouchi M., Akiyama M., Yoshida M., Ueda Y., 2008, ApJ, 675, 1076

Saxena A., Röttgering H. J. A., Rigby E. E., 2017, MNRAS, 469, 4083

Saxena A., et al., 2018a, MNRAS, 475, 5041

Saxena A., et al., 2018b, MNRAS, 480, 2733

Seifert W., et al., 2003, in Iye M., Moorwood A. F. M., eds, Society of Photo-Optical Instrumentation Engineers (SPIE) Conference Series Vol. 4841, Instrument Design and Performance for Optical/Infrared Ground-based Telescopes. pp 962–973, doi:10.1117/12.459494

Seymour N., et al., 2007, ApJS, 171, 353

Seymour N., et al., 2008, ApJ, 681, L1

Shimwell T. W., et al., 2017, A&A, 598, A104

Shimwell T. W., et al., 2019, A&A, 622, A1

Singh V., et al., 2014, A&A, 569, A52

Sobral D., et al., 2018, MNRAS, 477, 2817

Swarup G., Ananthakrishnan S., Kapahi V. K., Rao A. P., Subrahmanya C. R., Kulkarni V. K., 1991, Current Science, Vol. 60, NO.2/JAN25, P. 95, 1991, 60, 95

Taylor M. B., 2005, in Shopbell P., Britton M., Ebert R., eds,

Astronomical Society of the Pacific Conference Series Vol. 347, Astronomical Data Analysis Software and Systems XIV. p. 29

Tielens A. G. G. M., Miley G. K., Willis A. G., 1979, A&AS, 35, 153

Tingay S. J., et al., 2013, Publ. Astron. Soc. Australia, 30, e007

Vardoulaki E., et al., 2010, MNRAS, 401, 1709

Venemans B. P., et al., 2002, ApJ, 569, L11

Villar-Martin M., Tadhunter C., Clark N., 1997, A&A, 323, 21

Villar-Martín M., Humphrey A., De Breuck C., Fosbury R., Binette L., Vernet J., 2007a, MNRAS, 375, 1299

Villar-Martín M., Humphrey A., De Breuck C., Fosbury R., Binette L., Vernet J., 2007b, MNRAS, 375, 1299

Willott C. J., Rawlings S., Blundell K. M., Lacy M., 1999, MNRAS, 309, 1017

Willott C. J., Rawlings S., Blundell K. M., Lacy M., Hill G. J., Scott S. E., 2002, MNRAS, 335, 1120

Willott C. J., Rawlings S., Jarvis M. J., Blundell K. M., 2003, MNRAS, 339, 173

Wright E. L., et al., 2010, AJ, 140, 1868

Wylezalek D., et al., 2013, ApJ, 769, 79

Zirm A. W., Dey A., Dickinson M., Norman C. J., 2009, ApJ, 694, L31

van Breugel W., De Breuck C., Stanford S. A., Stern D., Röttgering H., Miley G., 1999, ApJ, 518, L61

van Haarlem M. P., et al., 2013, A&A, 556, A2

van Ojik R., Röttgering H. J. A., Carilli C. L., Miley G. K., Bremer M. N., Macchetto F., 1996, A&A, 313, 25

van Ojik R., Röttgering H. J. A., Miley G. K., Hunstead R. W., 1997, A&A, 317, 358

APPENDIX A: LONG-SLIT SPECTRA

Here we show the 1D spectra (observed frame) of all confirmed radio sources observed using three different facilities. The spectra are displayed with increasing redshift, and contain information about the source name, the redshift and the telescope used. Regions of strong skylines are marked by shaded boxes.

APPENDIX B: K-BAND IMAGES

Here we show the K band images for the subset of sources that were observed at NIR wavelengths. Overlaid on top of the K band image are radio contours at 1.4 GHz from Saxena et al. (2018a). The contours shown begin at 0.25 mJy, which is on average $3.5 - 5\sigma$, and are a geometric progression of $\sqrt{2}$, such that the flux density increases by a factor of 2 for every two contours.

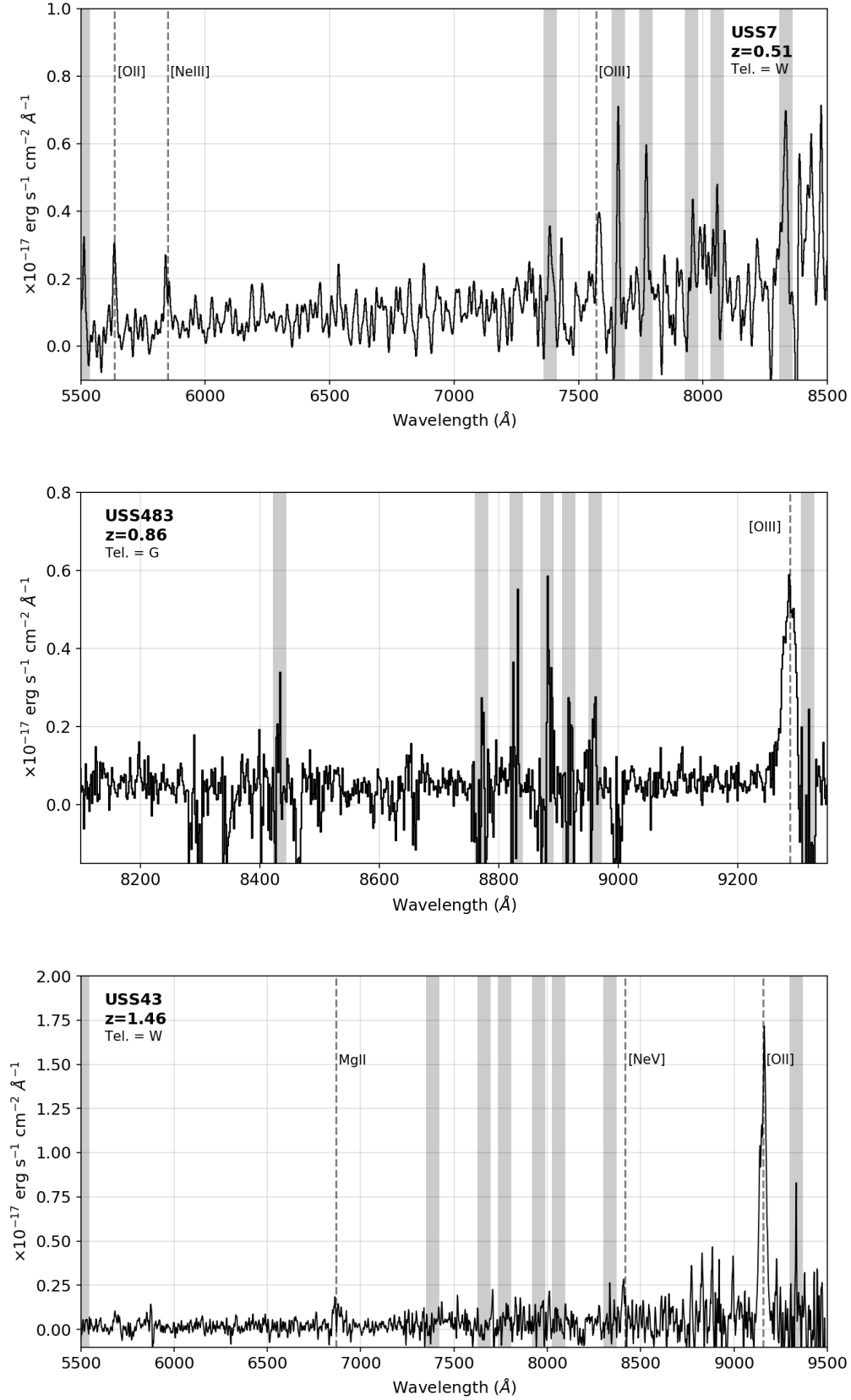This paper has been typeset from a TEX/LATEX file prepared by the author.

Figure A1. One dimensional spectra of all spectroscopically confirmed sources with the WHT, HET and Gemini. For clarity, we only show the relevant wavelength ranges for each spectrum. The shaded boxes indicate regions of strong contamination from atmospheric sky lines. Indicated in each spectrum is the, object name, redshift and telescope code (Tel.).
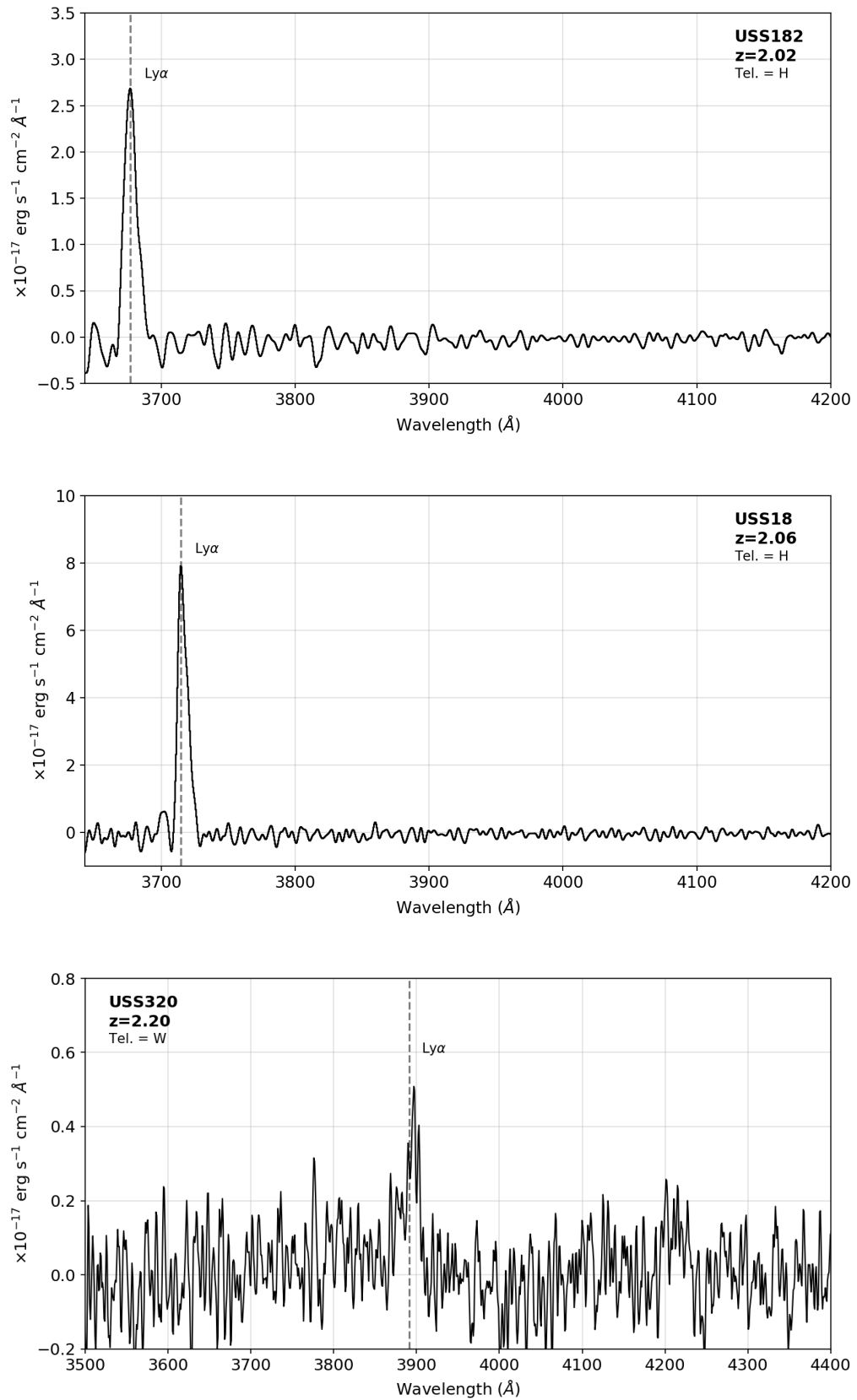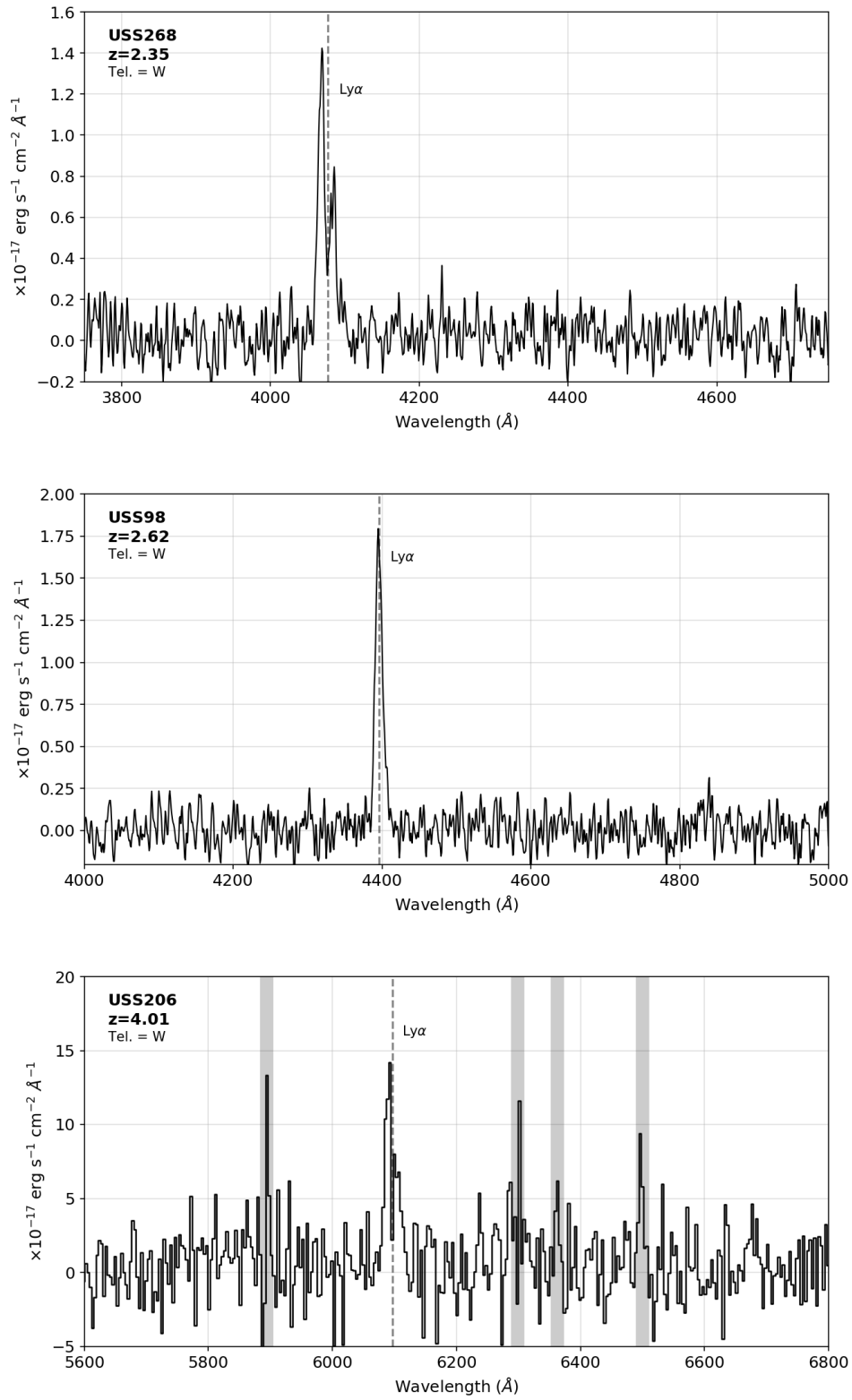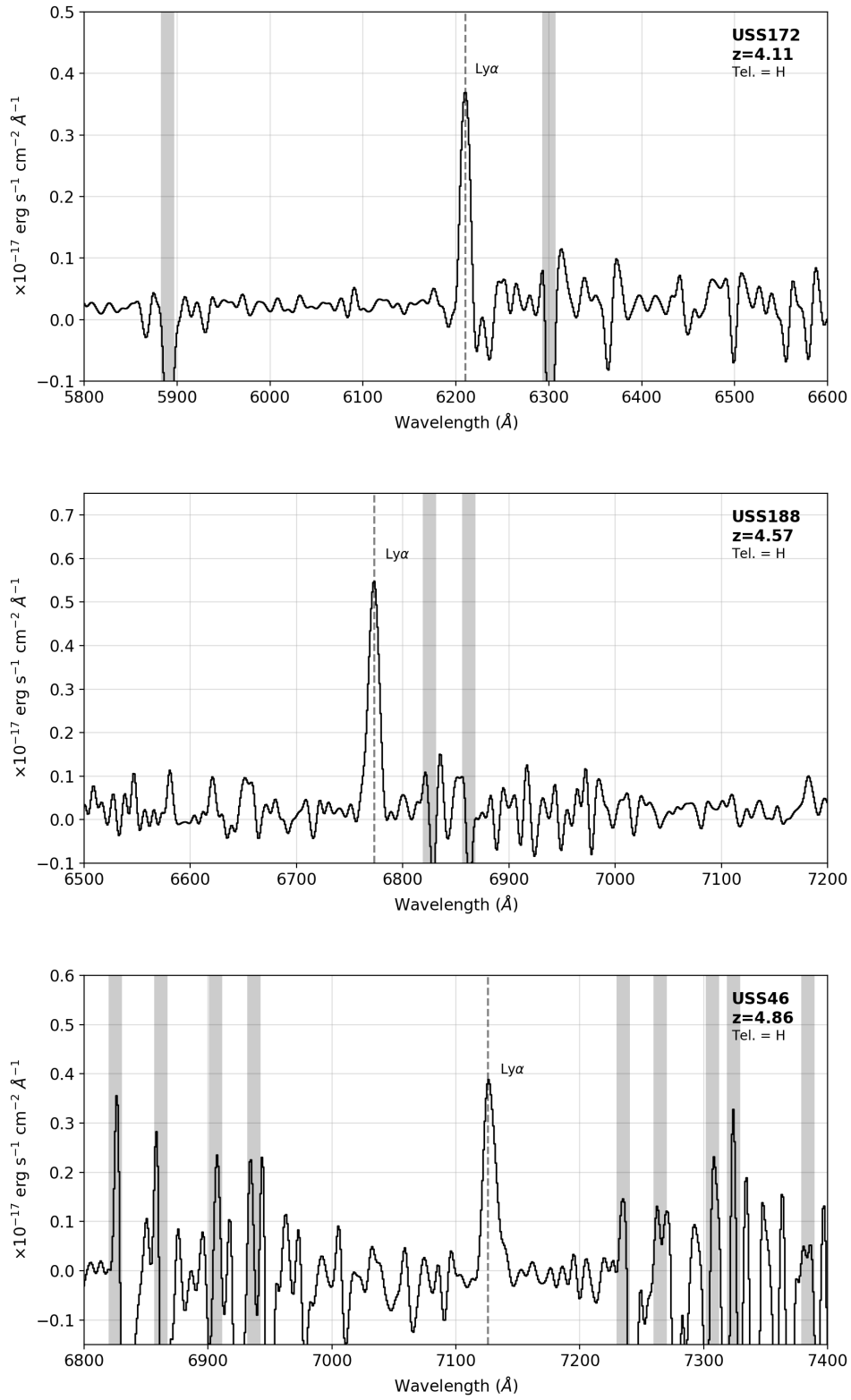
Figure A1. Continued.
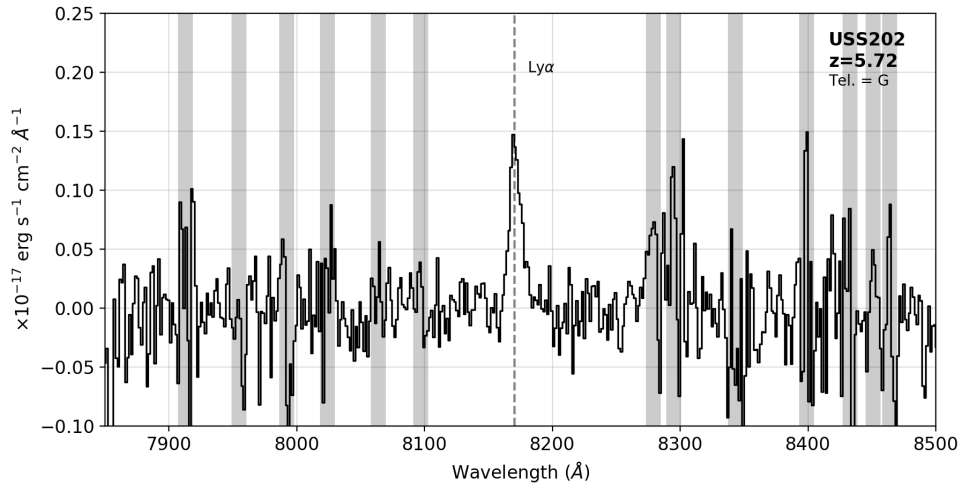
Figure A1. Continued.
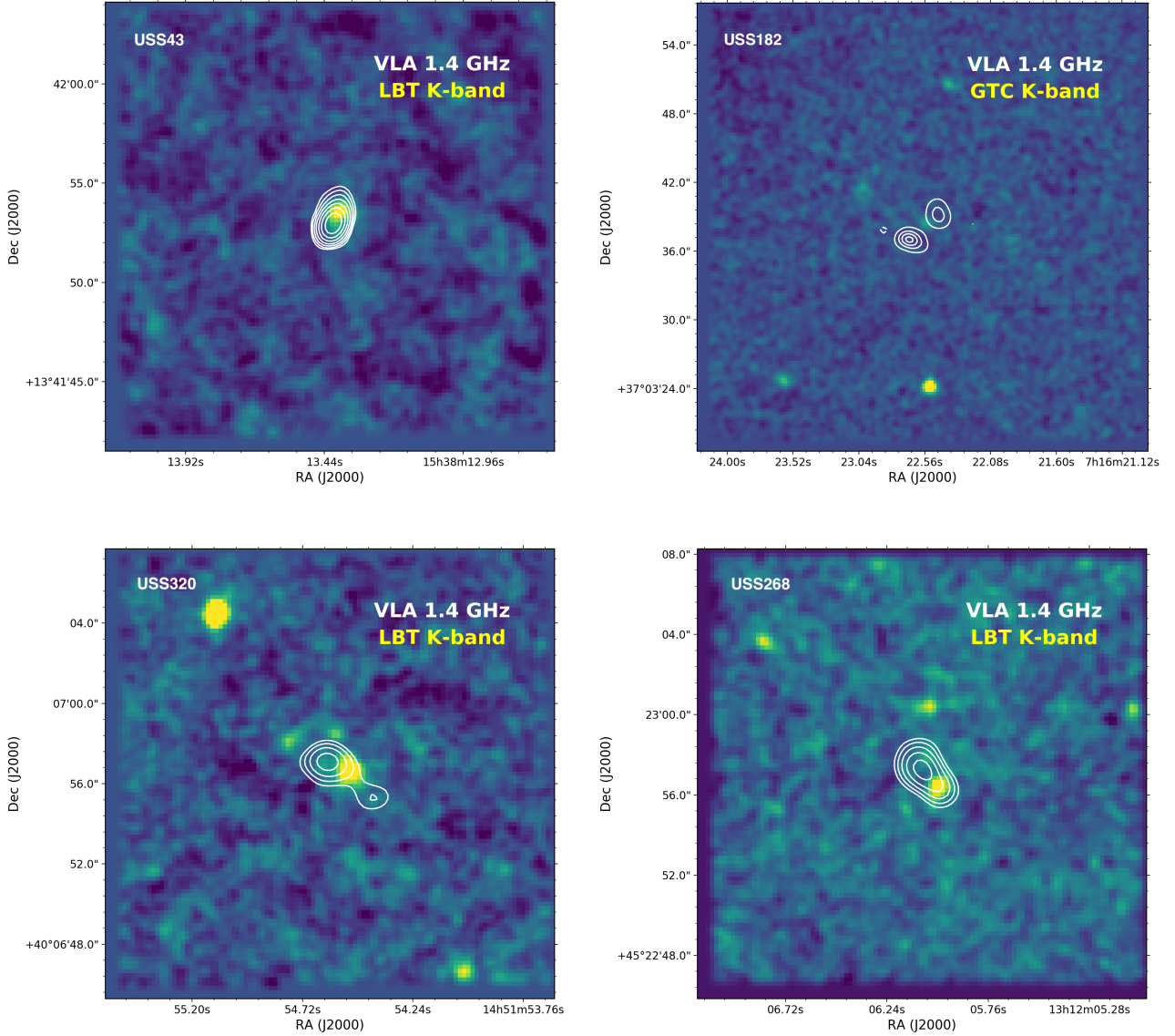
Figure A1. Continued.

Figure A1. Continued.

Figure B1. K-band images taken from the LBT and GTC of the host galaxies of the radio sources, with radio contours at 1.4 GHz from Saxena et al. (2018a) overlaid on top. The contours shown begin at 0.25 mJy, which is on average $3.5 - 5\sigma$, and are a geometric progression of $\sqrt{2}$, such that the flux density increases by a factor of 2 for every two contours.
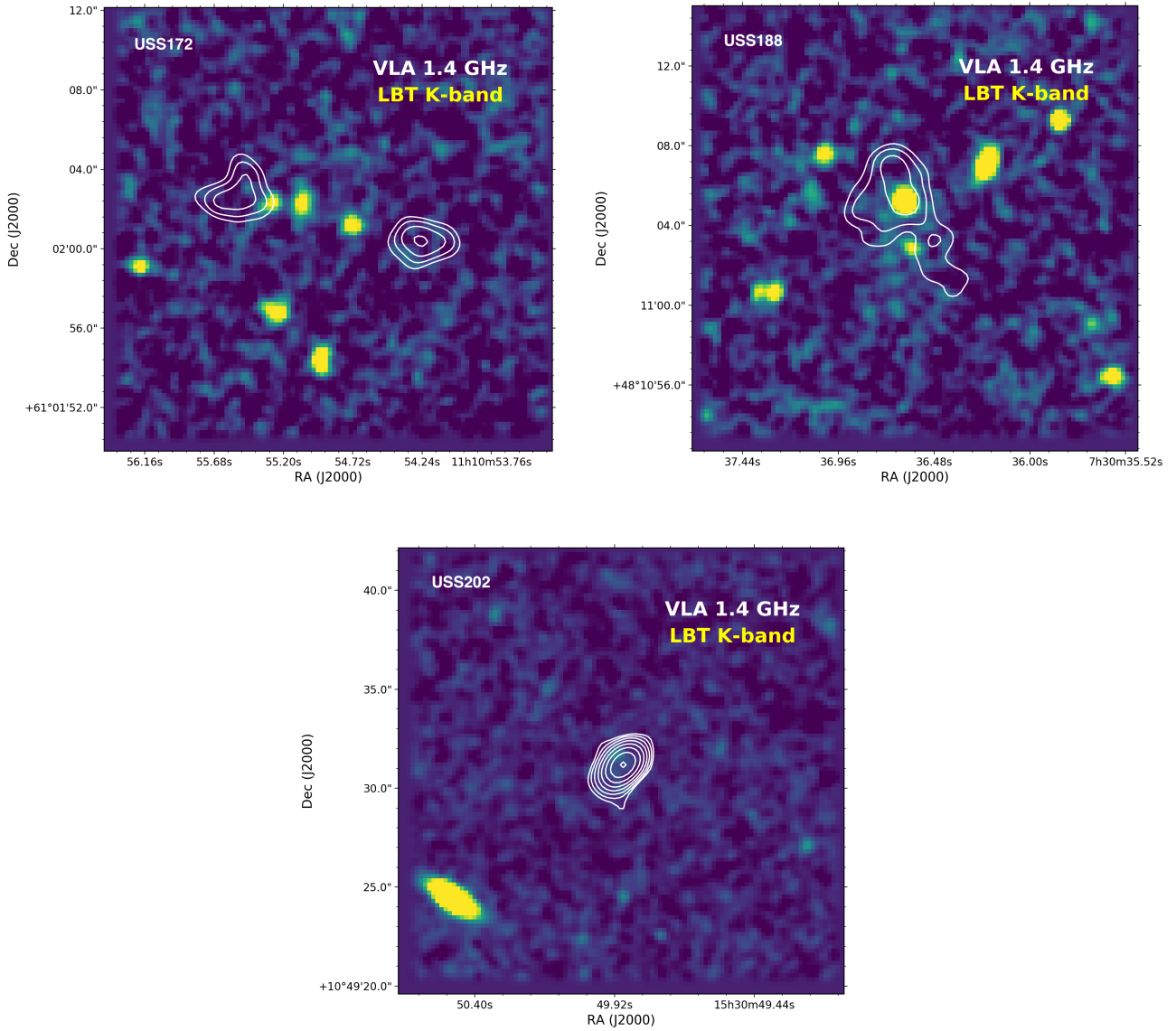
Figure B1. Continued.